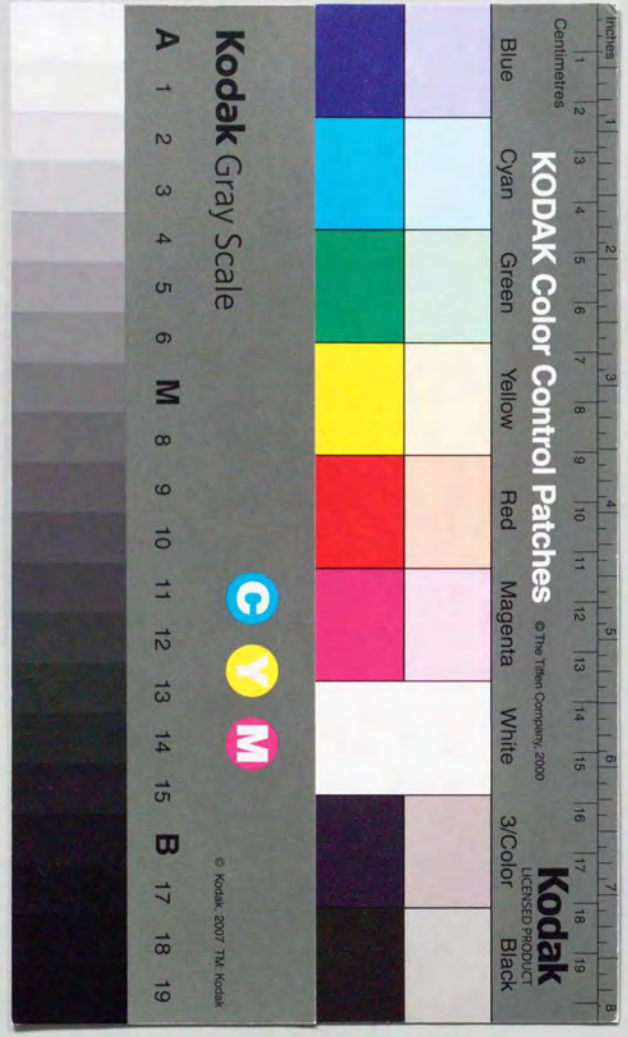

A Micromechanics-Based Continuum Theory for Localization Phenomena

マイクロメカニクスに基づく局所化現象に対する一連続体理論

Yoshiaki OKUI
奥井　義昭

January 1993
平成5年1月

Assoc. Prof. Hideyuki HORII
(Principal Advisor)

ABSTRACT

A MICROMECHANICS-BASED CONTINUUM THEORY FOR LOCALIZATION PHENOMENA

Yoshiaki OKUI

The conventional continuum theory is based on the constitutive equations that prescribe relations between the average stress and strain, valid when the local deformation is more or less uniform. However, when the deformation is localized, the effects of interaction among microdefects become important, and must be included in the formulation of any effective continuum theory. One promising way of establishing a continuum theory that can capture localization phenomena is to use micromechanics.

In this paper, a micromechanics-based continuum theory (named Interaction Field Theory, IFT) is proposed, which can model localization phenomena, such as shear failure in rocks or shear band formation in sands under compression. Special attention is placed on the effects of interaction among microdefects on determination of the evolution of microdefects. A new field variable (interaction field) that characterizes the effects of interaction among microdefects is introduced, and its governing integral equation is formulated. Although the technique is applicable to any material with any microstructure, for an illustration the theory is formulated and used to study the

behavior of geomaterials; namely, time-dependent and -independent deformation of brittle rocks and time-independent that of sands under compression.

Numerical results are given that illustrate the difference between the proposed theory and a continuum damage mechanics in which the interaction effects are not taken into account, as with conventional theories. It is confirmed that the proposed theory can describe the localization process as well as softening behavior, which are difficult to model by the continuum damage mechanics. Furthermore, numerical calculations are carried out in order to reproduce typical laboratory testing for geomaterials, such as short-term triaxial tests and creep tests under constant stress states. It is shown that the proposed theory is able to describe several features actually observed in laboratory tests; the transition from the shear failure mode to the axial splitting mode in triaxial tests of brittle rocks as the confine pressure is decreased and the typical shape of creep curves of brittle rocks.

Acknowledgment

I wish to express my deepest gratitude to my principal advisor, PhD. Hideyuki Horii (Assoc. Prof., University of Tokyo) for his invariable guidance and tutelage during my four years of research at University of Saitama. I have been very fortunate to have met PhD. Horii and if it had not been for his advice, I could not have write this dissertation. I would also like to thank Dr. Narioki Akiyama (present address: Prof., Nippon University), who had invited me to University of Saitama, and Dr. Hiroki Yamaguchi (Assoc. Prof., University of Saitama) for encouragement and numerous helpful suggestions.

After I finished my master course at University of Saitama in 1985, worked for four years as a structural engineer at Kawasaki Heavy Industries Ltd. I have joined the Structural Laboratory of the Department of Foundation Engineering at University of Saitama as a research associate from April 1989. When I had been invited to University of Saitama, I had intended to decline this offer because I could have no confidence in my own ability. Dr. Akiyama and Dr. Yamaguchi had advised that you should decide after you had met PhD. Horii. My first impressions of PhD. Horii are common-sense and trustworthy. (As far as I know, excellent scholars often have no common sense.) I had decided to come back to University of Saitama because of this impressions, which do not have been changed until now. At University of Saitama, Prof. Akiyama and Assoc. Prof. Yamaguchi have offered me comfortable and liberal environment, in which I could study everything I wanted to do.

I would like to thank Dr. Manabu Ito (Prof., University of Saitama), Dr. Masatugu Nagai (Assoc. Prof., Nagaoka University of Science and Technology), Mr. Mamoru

Izawa (Sumitomo Metal Industries Ltd.), Dr. Tetuo Iwakuma (Assoc. Prof., Tohoku University) and Dr. Tadashi Yamabe (Assoc. Prof., University of Saitama) for encouragement and kindly help. Dr. Nagai and Mr. Izawa were my bosses at Kawasaki Heavy Industries Ltd. and after my change to University of Saitama, they have treated me with kindness.

I would like to thank the following persons for valuable suggestions and their friendship: PhD. Muneo Hori (University of Tokyo), PhD. Eiki Yamaguchi (University of Tokyo), Dr. William Tanzo (University of Saitama) and Mr. Masahiko Osada (University of Saitama). In addition, I would like to thank to many students and Yurumu Matuhasi (laboratory engineer) for their help.

The financial support received from a Grant-in-Aid for Scientific Research of Japan's Ministry of Education is gratefully acknowledged.

Contents

List of Tables

List of Figures

Chapter 1

Introduction

1.1 Localization Phenomena

Localization phenomena are phenomena in which deformation or damage concentrates into one or more small zones in materials. Two types of localization phenomena can be distinguished: (1) localization due to stress concentration under certain boundary conditions and (2) localization from homogeneous stress states. A typical example of the former type of localization is unstable crack growth in brittle materials under tensile stress states. When the stress intensity factor at the tip of the crack attains its critical value—the fracture toughness, the crack extends abruptly without the increase of any external loading. This type of localization phenomena is relatively simple and engineering problems related to localization due to stress concentration are easily resolved by employing conventional theories, such as fracture mechanics. In the latter type of localization phenomena, firstly inelastic deformation or damage is distributed homogeneously over a large zone but later the inelastic deformation or damage concentrates into a relatively small zone as progressive evolution of damage. The localization

phenomena discussed in the present paper are this transitional type of localization; and in the following, the localization due to the stress concentration is not included in the sense localization phenomena are used in this present study.

The localization phenomena occur in a wide variety of materials: structural metals [Nadai, 1950], rocks [Friedman and Logan, 1973], concrete [Torrenti et al., 1989] and granular materials [Mandel et al., 1977]. For instance, a flat bar of mild steel under uniaxial tension exhibits thin lines which is inclined at an angle of about 45 deg with respect to the direction of tension. These lines, called "Lüders' lines" or simply "shear bands", quickly spread over the length of bar at the instant of the drop in the load at the yield point and their thickness increases. In shear bands, a large amount of the plastic shear is generated and the thickness of the bars becomes thin.

As an another example of the localization phenomena, failure of rocks under compressive stress state is considered. The failure modes of rock samples depend on the magnitude of the confining pressure and may be classified as follows: (1) axial splitting under uniaxial compression or low confining pressure, (2) brittle shear faulting and (3) ductile flow under a high confining pressure. The mechanism of the axial splitting results essentially from unstable extension of a single crack in the sample and the final plane of rupture is parallel to the direction of the maximum compression. The ductile flow exhibits no localized region of strain and cracking. On the other hand, the brittle shear failure belongs to the localization phenomena considered here. The final plane of shear faulting is also inclined with respect to the direction of the maximum compression. The shear faulting plane consists of highly density zones of microcracks whose orientations are almost parallel to the direction of the maximum compression [Wawersik and Brace, 1971; Hallbauer et al., 1973; Sprunt and Brace, 1974; Hadley, 1975; Tapponnier and Brace, 1976]. The process of localization of micro cracking into a narrow band is observed by means of optical microscopy [Hallbauer et al., 1973] and

acoustic emission [Yanagidani et al., 1985]. Hallbauer et al. reported that in the earlier loading stages the areas of high crack densities are confined to the central part of the specimen, but randomly distributed. With increasing axial stress, some of the localized areas appear to join into a plane which forms the macroscopic failure plane later. At axial stress close to the ultimate strength of the specimen this final plane is not yet clearly defined. Such shear faults are formed in natural rock masses by tectonic or gravitational possesses.

Probably the most important aspect of localization phenomena in engineering practice is the fact that the load carrying capacities of the material extensively depend on localization. As shown in above examples, the localization is a precursor of macroscopic failure and the stability of materials for external loading often changes at occurrence of localization. Because of the engineering significance and occurrence in various materials, many papers have been published on the mechanics of localization. Review of the development of theoretical work on this topic is given in the next section.

1.2 Previous Studies

1.2.1 Continuum Theory

The nonlinear response of engineering materials depends on the type, size, distribution and orientation of microdefects in the materials. With an increasing load, microdefects in a material evolve, and the effects of interaction among the microdefects become dominant, governing the process of macroscopic failure. For example, the macroscopic failure of brittle materials such as rock under compression consists of several stages: (1) nucleation and evolution of microcracks; (2) localization of microcracking; (3) formation of macroscopic fault due to coalescence of the localized microcracks. To establish

a theory for such mechanical behaviors of materials, it is important to take account of the influence of microdefects. It would seem natural to consider and model discrete microdefects using the method of micromechanics. However, consideration of the interaction effects of individual microdefects with a discrete model is not feasible for analyses of general problems with arbitrary boundary and loading conditions. It is therefore necessary to establish a continuum theory that describes the overall behavior of materials containing microdefects.

Continuum theories for mechanical behaviors of materials are divided into two different approaches: the phenomenological approach and the micromechanics-based approach. In the phenomenological approach, the relations between macroscopic quantities (e.g. the flow rule in plasticity or the evolution law of damage in phenomenological continuum damage mechanics) are based on relationship between macroscopic quantities obtained from experiments. In the micromechanics-based approach, the behavior of microdefects distributed in the material is generally considered to explain the mechanical behavior of the material. One of the issues of interest is whether or not a continuum theory can reproduce the process of localization phenomena.

Plasticity

While most phenomenological continuum theories do not reproduce localization phenomena, studies on plasticity have been carried out for the reproduction of localization phenomena, such as the diffuse neck of structural metal in a plane tensile test and the shear failure of brittle rock masses in compression. The theoretical description of shear bands can be traced back to the early work of Hill [1961]. In studying acceleration wave in elastoplastic solids, Hill presented equations for stationary wave, which are reduced to the condition of shear band localization for vanishing wave velocity. Hill and Hutchinson [1975] studied the localization problem of a rectangular block under

plane deformation. They consider a broad class of incrementally-liner incompressible materials whose behavior is characterized by the two instantaneous moduli. Rudnicki and Rice [1975] provide the general mathematical theory for analysis of shear band localization. The constitutive equations which are examined in the condition of localization are intended to model the behavior of brittle rock mass under compressive stress. It is shown that both a vertex-like structure of subsequent yield surfaces and non-normality strongly affect localization [see also Needleman, 1979].

In the above papers, the problem of localization phenomena is studied by applying bifurcation theory. The conditions under which a homogeneous deformation changes into a localized one is investigated. This bifurcation into a localized shear bands is not possible until the equations governing incremental equilibrium lose ellipticity. Special features are included in the constitutive models to reproduce localization phenomena through either (i) the vertex effects in the flow rule, (ii) the non-normality or (iii) the strain-softening. However, these theoretical works do not clarify the physical mechanism of localization phenomena, and predict only behavior at the onset of localization. Numerical methods are indispensable to follow the behavior in post-localized (bifurcation) regime. The complications of numerical analysis for localization problem will be discussed in section 1.2.2.

Continuum Damage Mechanics

In phenomenological Continuum Damage Mechanics (CDM), a set of continuous field variables that represent the damage of the material, called damage parameters or internal variables, is introduced without consideration of microscopic events. The mechanical property of the material at a certain state of damage is prescribed by the damage parameters. The evolution law that determines the value of the damage parameters for a given macroscopic stress or strain is deduced from the general frame-

work of thermodynamics or by simple fitting of experimental data. This concept was originally introduced by Kachanov [1958] for creep rupture of metals under uniaxial tension. Since then, extensive efforts have been made to apply phenomenological CDM to other phenomena or materials, such as multiaxial creep rupture [Murakami, 1983], creep-fatigue interaction [Chrzanowski, 1976], brittle fracture [Krajcinovic and Fonseka, 1981; Fonseka and Krajcinovic, 1981; Najar, 1987; Ashby and Sammis, 1990; Wohua and Valliappan, 1990a,b], brittle–ductile fracture [Dragon and Mróz, 1979], fatigue [Talreja, 1985; Chaboche and Lesne, 1988] and ductile fracture [Lemaitre, 1985; Chow and Wang, 1987]. Comprehensive review can be found in Chaboche [1988]. Although phenomenological CDM is effective for the reproduction of deformation behavior, it cannot predict localization phenomena.

Recently, Shi and Horii [1989] have investigated the evolution and interaction effects of the discrete system of microdefects to clarify the mechanism of strain localization in sand deformation. This theoretical work based on micromechanics has revealed that the dominant mechanism of localization is the effects of interaction among microdefects. The effects of interaction among microdefects are directly taken into account by considering discrete microdefects after the standard manner of micromechanics.

One promising way of establishing a continuum theory that can capture localization phenomena is to base it on micromechanics. In order to establish a continuum theory based on micromechanics, it is necessary to replace a heterogeneous material containing many microdefects with an equivalent continuum that exhibits the macroscopic behavior of the material. This procedure is called homogenization. Many mathematical techniques for homogenization have been proposed (see Hashin [1983] for literatures), such as averaging over the periodic structure or the representative volume element [Nemat-Nasser and Hori, 1989] and the self-consistent method [Budiansky and O'Connell, 1976; Horii and Nemat-Nasser, 1983]. These homogenization techniques

provide the overall stress-strain relation which reflects the effects of interaction among microdefects. However, it is not suitable for the formulation of a continuum theory that can reproduce localization phenomena, because a more or less uniform or periodic distribution of microdefects is assumed in most of these techniques. Although the effects of interaction on the evolution of microdefects seems to be more significant than that on the overall stress-strain relation, these homogenization techniques provide only the overall stress-strain relation at a certain state of microdefects.

One example of a micromechanics-based continuum theory is micromechanics-based CDM [Krajcinovic and Sumarac, 1989; Sumarac and Krajcinovic, 1989]. In this branch of CDM, the stress-strain relation of the equivalent continuum is derived from the average stress-strain relation of the heterogeneous material through the above-mentioned homogenization techniques, and the evolution law of damage is derived from considering the growth of microdefects. Like most phenomenological continuum theories, the conventional micromechanics-based CDM does not reproduce localization phenomena. This disadvantage occurs because, when the evolution of damage is evaluated, the interaction effects is not directly considered. The evolution law is derived for uniform evolution of microdefects.

1.2.2 Localization Limiter

To simulate behavior of materials up to complete localized state, in general, solutions of boundary value problems need to be obtained numerically. Even if the continuum theories which can reproduce localization phenomena are employed, the numerical solutions of problems for localization are fraught with serious complications. If the governing equations of the problems are discretized by finite element methods, overall responses such as relations between load and displacement depend on the size of elements used

for spatial discretization. This mesh dependency results from the fact that localization of deformation occurs in only one row of elements (in two dimensional problem) and the refinement of the mesh leads to vanishing size of localized region in the end.

To prevent this mesh dependency in numerical analysis, several methods which limit region of localization into finite size have been used. These methods, called "localization limiters", can be classified as follows [de Borst and Mühlhaus, 1991]:

(a) nonlocal model in which stress or strain is defined as an integral over a finite domain (integral limiter).

(b) strain gradient model in which strain is defined as derivatives of order higher than one (differential or gradient limiter).

(c) generalized continuum theory in which internal material length is originally introduced by considering microstructures in the material, such as Cosserat continuum theory.

(d) modeling materials with rate-dependent constitutive relation (rate limiter) [Lemonds and Needleman, 1986; Needleman, 1988]

Besides above mentioned methods, there are other methods which cannot predict the size of softening region but can simulate mesh independent relation between load and displacement:

(e) limiting the minimum size of the finite elements by considering the fact that constitutive relations are originally obtained by observation of relations between macroscopic quantities in finite size specimens.

(f) providing descending gradient of stress-strain relation in the post-peak regime as a function of mesh size.

In the following the methods from (a) to (c), which are relevant to the present study, are introduced.

Nonlocal theory

Eringen and co-workers [Eringen and Edelen, 1972; Inan and Eringen, 1991] propose a nonlocal theory with stress–strain and strain–displacement relations of the type

$$t_{ij}(\boldsymbol{x}) = \int_V \gamma(|\boldsymbol{x}-\boldsymbol{x}'|,\tau)\sigma_{ij}(\boldsymbol{x}')dV(\boldsymbol{x}'), \quad \cdots\cdots (1.1)$$

$$\sigma_{ij}(\boldsymbol{x}') = D_{ijkl}\varepsilon_{kl}(\boldsymbol{x}'), \quad \cdots\cdots (1.2)$$

$$\varepsilon_{ij}(\boldsymbol{x}') = \frac{1}{2}\{u_{i,j}(\boldsymbol{x}')+u_{j,i}(\boldsymbol{x}')\}, \quad \cdots\cdots (1.3)$$

where t_{ij} and u_i are the stress tensor and the displacement vector respectively; D_{ijkl} is the elastic tensor and γ is the attenuation function which depends on the distance $|\boldsymbol{x}-\boldsymbol{x}'|$ and a parameter τ which denotes the ratio of the internal characteristic length a to the external characteristic length l i.e.

$$\tau = c_0 a/l. \quad \cdots\cdots (1.4)$$

For example, when discussing a crack in crystals, the characteristic length a may be taken as a lattice parameter and l as half the length of the crack with a scale factor c_0.

In addition to the above equations, considering the equilibrium equation

$$t_{ij,j} = 0 \quad \cdots\cdots (1.5)$$

together with boundary conditions, theory of the nonlocal elasticity is formulated.

Various attenuation functions have been proposed in the literature by fitting the dispersion curves of plane wave of atomic lattice, for examples:

(a) One-dimensional problem

$$\gamma(|x|,\tau) = \begin{cases} \frac{1}{l\tau}(1-\frac{|x|}{l\tau}), & |x|<l\tau \\ 0, & |x|>l\tau \end{cases} \quad \cdots\cdots (1.6)$$

$$\gamma(|x|,\tau) = \frac{1}{2l\tau}exp(-|x|/l\tau), \quad \cdots\cdots (1.7)$$

$$\gamma(|x|,\tau) = \frac{1}{l\sqrt{\pi\tau}}exp(-x^2/l^2\tau), \quad \cdots\cdots (1.8)$$

(b) Two-dimensional problem

$$\gamma(|\boldsymbol{x}|,\tau) = \frac{1}{2\pi l^2\tau^2}K_0(\frac{(\boldsymbol{x}\cdot\boldsymbol{x})^{1/2}}{l\tau}), \quad \cdots\cdots (1.9)$$

where K_0 is the modified Bessel function.

$$\gamma(|\boldsymbol{x}|,\tau) = \frac{1}{\pi\tau l^2}exp(-\frac{\boldsymbol{x}\cdot\boldsymbol{x}}{l^2\tau}). \quad \cdots\cdots (1.10)$$

All the above expressions have the property that $\gamma(|\boldsymbol{x}-\boldsymbol{x}'|) \to \delta(|\boldsymbol{x}-\boldsymbol{x}'|)$ as $\tau \to 0$.

Recently, Bažant and co-workers [Bažant and Cabot, 1987; Droz and Bažant, 1989; Bažant, 1991] applied the nonlocal concept to the numerical analysis of strain–softening materials. As an example, they studied compression failure due to propagation of shear bands by finite element analysis. They used Mohr-Coulomb's plasticity and the strain–softening constitutive relation modeled through a negative value of the hardening modulus. As a localization limiter, they assumed that the yield limit is a function of a nonlocal plastic strain rate, such as

$$\dot{\varepsilon}^p_{ij}(\boldsymbol{x}) = \frac{1}{V_r(\boldsymbol{x})}\int_V \gamma(|\boldsymbol{x}-\boldsymbol{x}'|)\dot{\varepsilon}^p_{ij}(\boldsymbol{x}')dV(\boldsymbol{x}'), \quad \cdots\cdots (1.11)$$

$$V_r(\boldsymbol{x}) = \int_V \gamma(|\boldsymbol{x}-\boldsymbol{x}'|)dV(\boldsymbol{x}'), \quad \cdots\cdots (1.12)$$

in which the weighting (attenuation) function γ is Gaussian error density function

$$\gamma(|\boldsymbol{x}|) = exp(-\frac{k|\boldsymbol{x}|}{a}), \quad \cdots\cdots (1.13)$$

with $k = \sqrt{\pi}$ and $k = 2$ in one and two dimensional problem, respectively, and a is the internal characteristic length. They reported that if the element size is reduced smaller, the region of strain-softening and associated localization converges finite size and accordingly the numerical results do not depend on the element size. However mechanical meaning of the weighting function and the internal characteristic length is not clear, and the method of determination of the internal characteristic length is merely to fit numerical results to plausible values.

Strain gradient theory

In strain gradient theory [Triantafyllidis and Aifantis, 1986] the constitutive relation contains higher order derivatives of the strain. These higher order derivatives are generated due to nonlocality which means that the material property does not depend on only a point but also other points in the material. For example, when the material contains microstructure such as dislocations, microvoids and microcracks, the nonlocality occurs because of the effects of interaction among microstructures.

To demonstrate the relation between the nonlocal theory and the strain gradient theory, consider two material points $\boldsymbol{x}$ and $\boldsymbol{x}'$. The elastic tensor is assumed to have the nonlocality and denotes $D_{ijkl}(\boldsymbol{x}|\boldsymbol{x}')$. Then, stress at the point $\boldsymbol{x}$ is expressed as

$$\sigma_{ij}(\boldsymbol{x}) = \int_V D_{ijkl}(\boldsymbol{x}|\boldsymbol{x}')\varepsilon_{kl}(\boldsymbol{x}')dV(\boldsymbol{x}'), \quad \cdots\cdots (1.14)$$

where V is the volume of the material. When strain $\varepsilon_{kl}(\boldsymbol{x}')$ is expanded about $\boldsymbol{x}$ into a Taylor series, the stress strain relation become

$$\begin{aligned}\sigma_{ij}(\boldsymbol{x}) &= \int_V D_{ijkl}(\boldsymbol{x}|\boldsymbol{x}')\varepsilon_{kl}(\boldsymbol{x}')dV \\ &+ \int_V D_{ijkl}(\boldsymbol{x}|\boldsymbol{x}')(x'_p - x_p)\varepsilon_{kl,p}(\boldsymbol{x}')dV \quad \cdots\cdots (1.15)\end{aligned}$$

$$+ \int_V D_{ijkl}(\boldsymbol{x}|\boldsymbol{x}')(x'_p - x_p)(x'_q - x_q)\varepsilon_{kl,pq}(\boldsymbol{x}')dV + \cdots.$$

Obviously the strain gradient theory is a finite approximation of the nonlocal theory.

Coleman and Hodgdon [1985] studied shear bands in ductile materials and formulated rigid-plastic constitutive relation which exhibits strain softening after a certain amount of plastic flow. Their constitutive relation is of the following type:

$$\sigma = \varphi(\epsilon) - \alpha\Delta\epsilon \quad \cdots\cdots (1.16)$$

where Δ denotes a Laplacian and $\varphi(\epsilon)$ is a usual elastoplastic constitutive law and α is a coefficient having the dimension of a force. More recently, Triantafyllidis and Aifantis studied shear band formation of hyperelastic materials by adding a second deformation gradient term to the expression for the strain energy density. Both of these two studies predict not only the direction but also the thickness of shear bands.

Cosserat continuum theory

In a Cosserat continuum, a material point has three additional rotational degrees of freedom besides the three translatory ones in the classical continuum. These additional freedoms are introduced to express effects of rotation of particles in granular materials. According to introduction of the rotational freedoms, the constitutive relation has additional three equations which provide the relations between couple stress tensor m_i and curvature tensor κ_i,

$$m_i = M\kappa_i \qquad (i = 1, 2, 3) \quad \cdots\cdots (1.17)$$

where M is a bending modulus. When the bending modulus is normalized by a shear modulus G, $\sqrt{M/G}$ has dimension of length and is related to radius of particles as

internal characteristic length. This introduction of the characteristic length into the constitutive relation acts as the localization limiter.

Recently, Mühlhaus and Vardoulakis [1987] studied sand deformation with Cosserat's theory. They generalized J_2 deformation theory of plasticity and treated shear band formation in sand as a bifurcation problem. In the framework of classical bifurcation theory, it is not possible to predict the thickness of the shear band, since the formulation does not contain any physical property with the dimension of length. But, by employing Cosserat theory, they predicted the thickness of the shear band and showed a good agreement between theoretical predictions and experimental results.

1.3 Objectives of Present Study

The main object of the present study is to establish a micromechanics-based continuum theory which can reproduce the localization phenomena. In the proposed theory, the effects of interaction among microdefects are directly taken into account in the determination of the evolution of damage. To preserve information on the interaction effects among microdefects in the homogenization process, an additional field variable (interaction field) is introduced, and the governing integral equation for the interaction field is formulated. The introduction of the integral equation, called consistency equation, into the governing equations brings about the nonlocal feature of the constitutive relation. Although in the conventional nonlocal theories the justification of the nonlocality is merely checked by phenomenological consideration based on numerical simulations, in the present study it is aimed to formulate rigorously the attenuation function for the considered model of microdefects by means of micromechanics. The theory is general and applicable to any material with any microdefects. In this study, however, the present formulation is carried out for only the behavior of rocks and sands

under compressive stresses.

The organization of this paper is as follows:

- In Chapter 2, the general concept of the proposed theory is presented.
- The theory is formulated for the rate-independent behavior of rocks under compression in Chapter 3. To demonstrate the difference between conventional CDM based on micromechanics and the proposed theory, CDM is also formulated for the same problem. Numerical results are given which illustrate the difference between the proposed theory and CDM.
- In Chapter 4, the formulation for behavior of sands is presented and the applicability of the proposed theory for granular materials is discussed.
- In Chapter 5, a summary and conclusions are presented.

References

M. F. Ashby and C. G. Sammis [1990], The damage mechanics of brittle solids in compression. *Pure Appl. Geophys.*, (3):489–521.

Z. P. Bažant [1991], Why continuum damage is nonlocal: micromechanics arguments. *J. Eng. Mech., ASCE*, 117(5):1070–1087.

Z. P. Bažant and G. P. -Cabot [1987], Modeling of distributed damage by nonlocal continuum with local strain. In A. R. Luxmoore et al., editors, *4th Int. Conf. on Numerical Methods in Fracture Mechanics*, pages 411–432, Pineridge Press, Swansea.

B. Budiansky and R. J. O'Connell [1976], Elastic moduli of a cracked solid. *Int. J. Solids Structures*, 12:81–97.

J. L. Chaboche [1988], Continuum damage mechanics: part 1-general concepts. *J. Appl. Mech. ASME*, 55:59–64.

J. L. Chaboche [1989], Phenomenological aspects of continuum damage mechanics. *Theoretical and Applied Mechanics*, 41–56.

J. L. Chaboche and P. M. Lesne [1988], A non-linear continuous fatigue damage model. *Fatigue Fract. Engng. Mater. Struct.*, 11(1):1–17.

C. L. Chow and J. Wang [1987], An anisotropic theory of continuum damage mechanics for ductile fracture. *Engineering Fracture Mechanics*, 27(5):547–558.

M. Chrzanowski [1976], Use of the damage concept in describing creep-fatigue interaction under prescribed. *Int. J. Rock Mech. Min. Sci. Geomech. Abstr.*, 18:69–73.

B. D. Coleman and M. L. Hodgdon [1985], On shear bands in ductile materials. *Archs. Rational Mech. Anal.*, 90:219–247.

R. de Borst and H.-B. Mühlhaus [1991], Continuum models for discontinuous media. In J. G. M. van Mier, J. G. Rots, and A. Bakker, editors, *Fracture Processes in Concrete, Rock and Ceramics*, pages 601–618. E. & F. N. Spon, London.

A. Dragon and Z. Mróz [1979], A continuum model for plastic–brittle behaviour of rock and concrete. *Int. J. Engng. Sci.*, 17:121–137.

P. Droz and Z. P. Bažant [1989], Nonlocal analysis of stable states and stable paths of propagation of damage shear bands. In J. Mazars and Z.P. Bažant, editors, *Cracking and Damage: Strain Localization and Size Effect*, pages 415–425, Elsevier, New York.

A.C. Eringen and D.G.B. Edelen [1972], On nonlocal elasticity. *Int. J. Engng. Sci.*, 10:233–248.

G. U. Fonseka and D. Krajcinovic [1981], The continuous damage theory of brittle materials: part 2 uniaxial and plane response modes. *J. of Appl. Mech.*, 48:816–824.

M. Friedman and J.M. Logan [1973], Luders' bands in experimentally deformed sandstone and limestone. *Geol. Soc. America Bulletin*, 84:1465–1476.

K. Hadley [1975], Comparison of calculated and observed crack densities and seismic velocities in Westerly granite. *J. Geophys. Res.* , 81(20):3184–3494.

D.K. Hallbauer, H. Wagner and N. G. W. Cook [1973], Some observations concerning the microscopic and mechanical behaviour of quartzite specimens in stiff, triaxial compression tests. *Int. J. Rock Mech. Min. Sci. & Geomech. Abstr.*, 10:713–726.

Z. Hashin [1983], Analysis of composite materials– a survey. *J. Appl. Mech. ASME*, 50:481–505.

R. Hill and J. W. Hutchinson [1975], Bifurcation phenomena in the plane tension test. *J. Mech. Phys. Solids*, 23:239–264.

H. Horii and S. Nemat-Nasser [1983], Overall moduli of solids with microcracks: load-induced anisotropy. *J. Mech. Phys. Solids*, 31(2):155–177.

E. Inan and A.C. Eringen [1991], Nonlocal theory of wave propagation in thermoelastic plate. *Int. J. Engng. Sci.*, 29(7):831–843.

L.M. Kachanov [1958], On the time to failure under creep conditions. *Izv. Akad. Nauk. SSR, Otd. Tekhn. Nauk*, (8):26–31.

D. Krajcinovic and G. U. Fonseka [1981], The continuous damage theory of brittle materials: part 1 general theory. *J. of Appl. Mech.*, 48:809–815.

D. Krajcinovic and D. Sumarac [1989], A mesomechanical model for brittle deformation processes: part 1. *J. of Appl. Mech.*, 56:51–56.

J. Lemaitre [1985], A continuous damage mechanics model for ductile fracture. *Journal of Engineering Materials and Technology*, 107:83–89.

J. Lemonds and A. Needleman [1986], Finite element analyses of shear localization in rate and temperature dependent solids. *Mechanics of Materials*, 5:339–361.

G. Mandel, L.N.J. de Jong and A. Maltha [1977], Shear zone in granular Material. *Rock Mech.*, 9:95–144.

H. -B. Mühlhaus and I. Vardoulakis [1987], The thickness of shear bands in granular materials. *Géotechnique*, 37(3):271–283.

S. Murakami [1983], Notion of continuum damage mechanics and its application to anisotropic creep damage theory. *Journal of Engineering Materials and Technology*, 105:99–105.

A. Nadai [1950], *Theory of Flow and Fracture of Solids* , chap. 19, McGraw-Hill.

J. Najar [1987], Continuous damage of brittle solids. In D. Krajcinovic and J. Lemaitre, editors, *Continuum Damage Mechanics: Theory and Applications*, pages 231–294, Springer-Verlag, Wien, New York.

A. Needleman [1979], Non-normality and bifurcation in plane strain tension and compression. *J. Mech. Phys. Solids*, 27:231–254.

A. Needleman [1988], Material rate dependence and mesh sensitivity in localization problems. *Computer Methods in Applied Mechanics and Engineering*, 67:69–85.

S. Nemat-Nasser and H. Hori [1989], Elastic solids with microdefects. In G. J. Weng, M. Taya, and H. Abe, editors, *Micromechanics and Inhomogeneity*, pages 297–320, Springer-Verlag.

J. W. Rudnicki and J. R. Rice [1975], Conditions for the localization of deformation in pressure-sensitive dilatant materials. *J. Mech. Phys. Solids*, 23:371–394.

Z.-H. Shi and H. Horii [1989], Microslip model of strain localization in sand deformation. *Mech. Mater.*, 8:89–102.

E. S. Sprunt and W. F. Brace [1974], Direct observation of microcavities in crystalline rocks *Int. J. Rock Mech. Min. Sci. & Geomech. Abstr.*, 11:139–150.

D. Sumarac and D. Krajcinovic [1989], A mesomechanical model for brittle deformation processes: part 2. *J. of Appl. Mech.*, 56:57–62.

R. Talreja [1986], A continuum mechanics characterization of damage in composite materials. *Proc. R. Soc. Lond.*, 399:195–216.

P. Tapponnier and W. F. Brace [1976], Development of stress-induced microcracks in Westerly Granite. *Int. J. Rock Mech. Min. Sci. & Geomech. Abstr.* , 13:103–112.

J.M. Torrenti, J. Desrues, P. Acker and C. Boulay [1972], Application of stereophotogrammetry to the strain localization in concrete compression. In J. Mazars and Z.P. Bažant editors, *Cracking and Damage: Strain Localization and Size Effect* , pages 30–41, Elsevier, London.

N. Triantafyllidis and E. C. Aifantis [1986], A gradient approach to localization of deformation. I. hyperelastic materials. *J. Elasticity*, 16:225–237.

V. Tvergaard, A. Needleman, and K. K. Lo [1981], Flow localization in the plane strain tensile test. *J. Mech. Phys. Solids*, 29(2):115–142.

W. R. Wawersik and W. F. Brace [1971], Post-failure behavior of a granite and diabase. *Roch Mechanics*, 3:61–85.

Z. Wohua and S. Valliappan [1990a], Analysis of random anisotropic damage mechanics problems of rock mass: part I – Probabilistic simulation. *Roch Mech. and Roch Engng.*, 23:91–112.

Z. Wohua and S. Valliappan [1990b], Analysis of random anisotropic damage mechanics problems of rock mass: part II – Statistical estimation. *Roch Mech. and Roch Engng.*, 23:241–259.

Chapter 2

Interaction Field Theory

In this chapter, the Interaction Field Theory (IFT) is introduced, which is a micromechanics-based continuum theory with special relevance to the effects of interaction. To illustrate the main concept of the theory, a comparison is made between the proposed theory and a CDM that is also based on micromechanics. In the following, only the micromechanics-based CDM is considered, and is referred to simply as CDM.

Figure 2.1 illustrates the micromechanics-based continuum theory for description of the behavior of a body subjected to the evolution of microdefects (microcracks in the illustration). Heterogeneous material containing many microcracks is modeled as an equivalent continuum. The usual equilibrium equation and the strain–displacement relationship are satisfied. A micromechanics-based constitutive equation, which gives the relation between the stress and strain at a point in the body, is constructed. We consider the globally uniform deformation of the material with microcracks. The relation between the average stress and strain is obtained by considering the behaviors of microcracks and is assumed to prescribe the material behavior at a given point in the body. The microcracks evolve as the deformation proceeds. Their evolution is

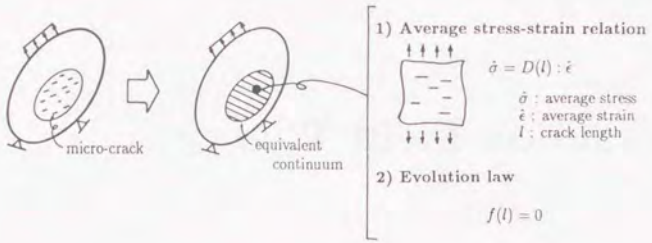

Figure 2.1 Micromechanics-based continuum theory.

determined by an evolution law.

Different versions of the micromechanics-based continuum theory are considered with different types of the homogenization procedure and evolution law. Here, a CDM and IFT are introduced. In the CDM, the evolution law is simply deduced by considering an infinite body with a single microcrack under average stress at infinity; see Fig. 2.2(a). The direct effects of interaction among microcracks are not taken into account, since only a single microcrack is considered. Thus, the evolution law depends only on local average stress at that point. In IFT, on the other hand, a new field variable called the interaction field is introduced to take account of the direct effects of interaction in the determination of the evolution of microcracks. The idea is based on the method of pseudotraction [Horii and Nemat-Nasser, 1985], which is a method to evaluate the interaction effects among discrete microdefects. The generalization of the method from a discrete system to the continuum leads to the tensor field that

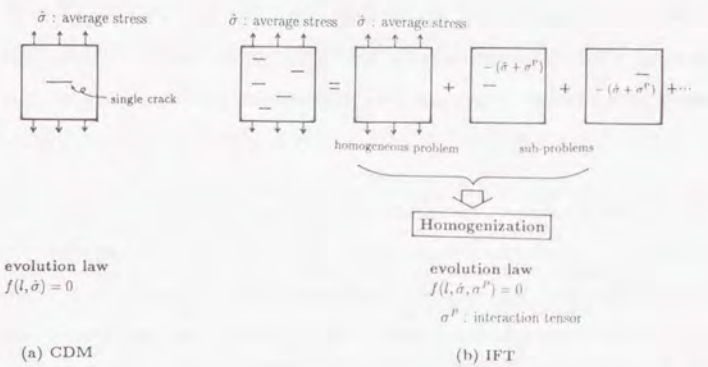

Figure 2.2 Comparison between CDM with Interaction Field Theory.

represents the interaction effects of distributed microdefects.

To introduce the idea, consider a body with many discrete microcracks. The problem is decomposed into a homogeneous problem and subproblems, each of which contains only one microcrack. To satisfy the traction-free condition along microcracks in the original problem, the average stress plus pseudotraction with the sign changed are applied on the surface of each microcrack.

The pseudotraction is to be determined such that the condition is satisfied when the homogeneous problem and the subproblems are superimposed. Pseudotraction $\sigma^{P\alpha}$ of microcrack α should equal the summation of tractions on microcrack α created by other microcracks in other subproblems. Hence, the pseudotraction is understood as the interaction effects at microcrack α from all other microcracks. If the evolution of microcrack α is considered in subproblem α, the direct interaction effects from all

other microcracks are through pseudotraction $\sigma^{P\alpha}$. When we introduce a homogenization from the discrete microcracks to the continuously distributed microcracks, the pseudotraction is transformed into the interaction field that is a tensor field of stress dimension. Then, the evolution law at a point becomes a function of both the average stress and the interaction field, and the evolution of microcracks depends on the direct interaction effects.

In the discrete system, the pseudotraction, which is a function defined along the microcrack, is expanded into Taylor series. Their coefficients are determined from the consistency condition that ensures the satisfaction of the traction-free condition. By homogenization from a discrete system to the continuum, the consistency condition is reduced to the integral equation for the interaction field. The evolution of microcracks and the deformation of the material are obtained by solving (1) the equilibrium equation, (2) the strain–displacement equation, (3) the stress–strain relationship, (4) the evolution law and (5) the consistency equation.

In this chapter, only the idea of IFT is introduced. In the next chapter, a theory is formulated for material behavior due to crack growth under compression to describe the IFT in detail.

References

H. Horii, K. Sahasakmontri and Y. Okui [1991], Overall moduli of cracked solid and parameter for crack geometry. *J. Struct. Engng.* , 37A:459–464, in Japanese.

Y. Okui, H. Horii and N. Akiyama [1992], A continuum theory for brittle materials under compression. *J. Struct. Engng.* , 38A:351–359, in Japanese.

Y. Okui, H. Horii and N. Akiyama [1992], A continuum theory based on Micromechanics for interacting damage. In M.H. Aliabaddi, D.J. Cartwright and H. Nisitani, editors, *Proc. of 2nd Int. Conf. on Computer-Aided Assessment and Control of Localized Damage, Localized Damage II* , Vol.1, pages 439–451, Elsevier, London.

Y. Okui, H. Horii and N. Akiyama [1992], A micromechanics-based continuum theory for strain localization and softening under compression. In Z.P. Bažant editor, *Proc. of 1st Int. Conf. on Fracture Mechanics of Concrete Structures,* , pages 275–280, Elsevier, London.

Y. Okui, H. Horii and N. Akiyama [1993], A continuum theory for solids containing microdefects. *Int. J. Engng. Sci.* , Accepted.

H. Horii and S. Nemat-Nasser [1985], Elastic fields of interacting inhomogeneities. *Int. J. Solids Structures*, 21(7):731–745.

Chapter 3

Formulation for Behavior due to Crack Growth under Compression

3.1 Introduction

As introduced previously, the formulation of IFT is carried out for rate-independent behaviors of brittle materials with microdefects under compression. Specifically, the behavior is observed in geomaterials such as rocks under low temperature and adequate magnitude of the confining pressure. In general, the inelastic deformation of rocks depends on the strain rate [Schock and Heard, 1974] and exhibits ductile behavior under high confining pressure [Edmond and Paterson, 1971; Barton, 1976]. However, we limit the scope of the present formulation to the above case since in the majority of engineering problems the behaviors of rocks are regarded as brittle and rate-independent.

In section 3.2, a model of microdefects in rocks under compression is introduced and the fundamental properties of the model are examined. In section 3.3, the interaction effects among the microdefects are discussed by considering the boundary value problem of an elastic medium containing two microdefects. The governing equations of IFT is formulated through the homogenization of the elastic medium with many microdefects in section 3.4. To illustrate the differences between the proposed theory and conventional CDM, a CDM based on micromechanics is formulated for the same problem in section 3.5. In section 3.6, the numerical results of both theories are presented. In addition, the strengths of actual rocks under compression are predicted with the proposed theory.

3.2 A Model of Crack Growth under Compression

The mechanical behaviors of brittle solids such as rock under compression are known to be governed by the growth of cracks. Microscopic observations of rocks [Wawerisk and Brace, 1971; Hallbauer et al., 1973 Kirby and Kronenberg, 1984], especially with a scanning electron microscope [Sprunt and Brace, 1974; Hadley, 1975; Tapponnier and Brace, 1976; Kranz, 1979], reveal detailed information about initial defects and load-induced cracks, such as length, density, aspect ratio and orientation. According to these observations, load-induced cracks nucleate at initial defects, such as grain boundaries or crack-like, low aspect ratio cavities. All load-induced cracks are almost parallel to the direction of the maximum compression. These load-induced cracks are interpreted as tension cracks caused by sliding deformation along the inclined initial defects.

To represent this behavior of crack growth under compression, a micromechanics model has been proposed, as shown in Fig. 3.1(a) [Moss and Gupta, 1982; Horii and

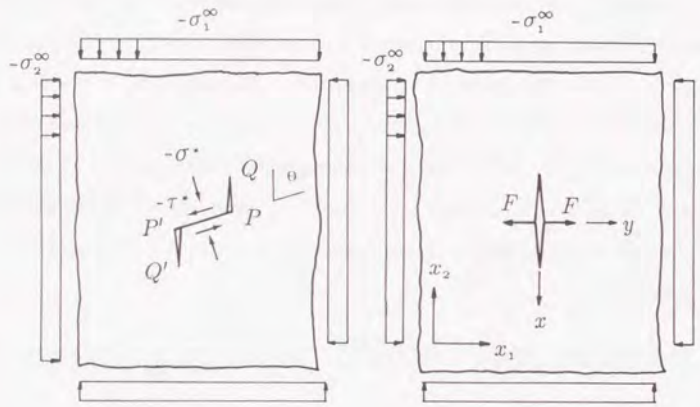

(a) (b)

Figure 3.1 Microdefect of rock under compression.

Nemat-Nasser, 1985; Ashby et al., 1986; Nemat-Nasser and Obata, 1988]. An initial defect PP' of length $2c_0$ undergoes frictional sliding under the action of far-field principal stresses σ_1^∞ and σ_2^∞ (positive in tension). Frictional sliding along the initial defect PP' induces the nucleation and growth of the tension cracks PQ and $P'Q'$ at the tips of the initial defect PP'. It is assumed that the initial defect is closed during the process of crack growth, and that the initial defect slides with a constant frictional coefficient μ. Thus, the following boundary condition must be satisfied on the initial defect PP':

$$\left.\begin{aligned} u_n^+ &= u_n^-, \\ \tau^{*+} &= \tau^{*-} = \mu\sigma^*, \end{aligned}\right\} \quad \cdots\cdots (3.1)$$

where u_n is the displacement in the direction normal to the initial defect and the superscript plus and minus stand for the quantity on the upper and lower surfaces of the initial defect, respectively. The solution of the problem shown in Fig. 3.1(a) is obtained by the numerical method. The closed form solution of this problem, however,

is not available.

A further simplified model is considered, as shown in Fig. 3.1(b) [Horii and Nemat-Nasser, 1985, 1986]. The straight crack of length $2l$ is parallel to the direction of the maximum compressive stress σ_1^∞. The effect of the sliding of the initial defect with normal stress σ^* and shear stress τ^*, due to the far-field principal stresses, is modeled as a pair of concentrated forces F at the center of the crack:

$$F = 2c_0(-\tau^* + \mu\sigma^*)\sin\theta = -c_0(\lambda_1\sigma_1^\infty - \lambda_2\sigma_2^\infty), \quad \cdots\cdots (3.2)$$

where c_0 is half the length of the initial defect,

$$\left.\begin{aligned} \lambda_1 &= \sin\theta\{\sin 2\theta - \mu(1-\cos 2\theta)\}, \\ \lambda_2 &= \sin\theta\{\sin 2\theta + \mu(1+\cos 2\theta)\}, \end{aligned}\right\} \quad \cdots\cdots (3.3)$$

μ is the coefficient of friction and θ is the angle of the initial defect. Figure 3.2 shows the relations between the coefficients λ_i, $(i = 1, 2)$ and the angle of the initial defect θ for the various coefficients of friction. Both of the coefficients λ_i reach the maximum values at about $\theta = 45$ deg.

From equation (3.2), the relation between the normalized magnitude of the concentrated forces $-F/(c_0\sigma_2^\infty)$ and stress ratio $R = \sigma_1^\infty/\sigma_2^\infty$ is expressed by

$$\frac{-F}{c_0\sigma_2^\infty} = \lambda_1 R - \lambda_2, \quad \cdots\cdots (3.4)$$

and this relation is plotted in Fig. 3.3 for the frictional coefficient $\mu = 0.3$. With the increase in the stress ratio, the normalized magnitude of the concentrated forces increases, which makes the microdefect illustrated in Fig. 3.1 grow. Within the cases shown in Fig. 3.2, the normalized magnitude of the forces in case $\theta = 45$ deg is maximum in all range of the stress ratio, and consequently it means that the tension cracks

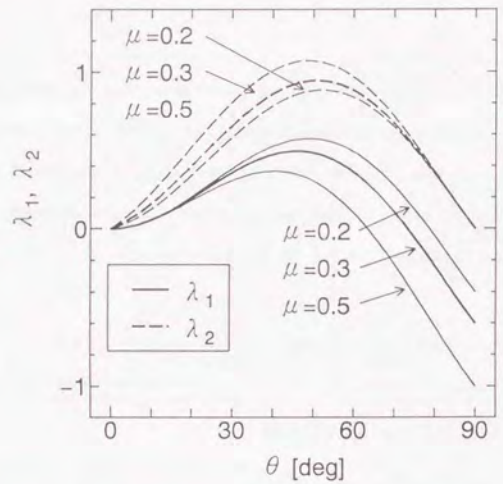

Figure 3.2 Variations of the coefficients λ_1 andλ_2 vs crack angle θ for various frictional coefficients.

from the tips of the initial defect with the angle $\theta = 45$ deg are most likely to grow. In addition, the microdefect cannot grow under $R < 1.8$ because of the negative value of the normalized concentrated forces, which means the initial defect does not slide. Thus, when the value of the concentrated forces defined by equation (3.2) is negative, the concentrated forces are assumed to be zero.

To understand fundamental response of this model, consider the evolution problem of the microdefect model under external loading. The condition of microdefect extension is assumed to follow the Griffith's criterion:

$$\left.\begin{array}{ll} \delta l \geq 0, & \text{if} \quad K_I = K_c, \\ \delta l = 0, & \text{if} \quad K_I < K_c, \end{array}\right\} \cdots\cdots (3.5)$$

where K_I is the mode I stress intensity factor of the tips of the microdefect and K_c is the

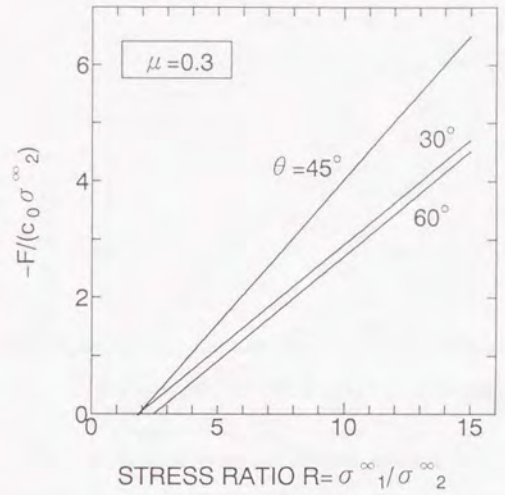

Figure 3.3 Relations between normalized concentrated forces $-F/(c_0\sigma_2^\infty)$ and stress ratio $\sigma_1^\infty/\sigma_2^\infty$ for the frictional coefficient $\mu = 0.3$.

fracture toughness of the matrix. The mode I stress intensity factor of the considered microdefect model is given by

$$K_I = \sqrt{\pi l}\sigma_2^\infty + \frac{F}{\sqrt{\pi l}}. \cdots\cdots (3.6)$$

Thus, the evolution equation $K_I - K_c = 0$ is expressed by the following normalized form:

$$\sqrt{l^*} - \frac{1}{\pi\sqrt{l^*}}(\lambda_1 R - \lambda_2) - K_c^* = 0, \cdots\cdots (3.7)$$

where the normalized length of the microdefect l^* and fracture toughness K_c^* are defined by $l^* = l/c_0$ and $K_c^* = K_c/(\sqrt{\pi c_0}\sigma_2^\infty)$, respectively. Equation (3.7) becomes the quadratic equation for $\sqrt{l^*}$, and the roots of the equation are given by

$$\sqrt{l^*} = \frac{1}{2}(K_c^* \pm \sqrt{D}), \quad \cdots\cdots (3.8)$$

where

$$D = K_c^{*2} + \frac{4}{\pi}(\lambda_1 R - \lambda_2). \quad \cdots\cdots (3.9)$$

The responses of the microdefect are classified into the following two cases: (a) compressive confining pressure, and (b) tensile confining pressure.

For the case of the compressive confining pressure, since the positive root of $\sqrt{l^*}$ is the only case of the positive sign in equation (3.8), the expression of the normalized length of the microdefect is

$$l^* = \frac{1}{4}\{K_c^* + [K_c^{*2} + \frac{4}{\pi}(\lambda_1 R - \lambda_2)]^{0.5}\}^2, \quad \cdots\cdots (3.10)$$

and this relation for $\mu = 0.3$ and $\theta = \pi/4$ is plotted in Fig. 3.4. The microdefect grows as the stress ratio increases, and the maximum stress ratio does not exists.

On the other hand, for the case of tensile pressure, there are two roots in the range of the stress ratio which satisfies $D > 0$, and the relation between the stress ratio and the normalized length of the microdefect is shown in Fig. 3.5. Although the stress ratio increases as the microdefect grows for the beginning of the loading stages, the stress ratio reaches its maximum value R_c, and decreases with the increase in the normalized length of the microdefect. This behavior means that, if the material containing the microdefect is loaded with the load control method, the microdefect grows unstably and the material fails catastrophically. From the condition $D = 0$, the maximum stress ratio R_c is given by

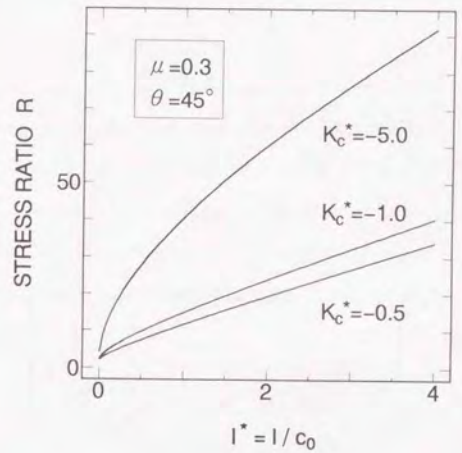

Figure 3.4 Evolution of a single microdefect under compressive confining pressure ($\sigma_2^\infty < 0$) for various normalized fracture toughness.

$$R_c = -\frac{\pi}{4\lambda_1}K_c^{*2} + \frac{\lambda_2}{\lambda_1}, \qquad \text{at} \quad l^* = \frac{K_c^{*2}}{4}. \quad \cdots\cdots (3.11)$$

As a result of the evolution problem of the single microdefect, it is shown that the unstable evolution of the microdefect does not take place unless the confining pressure is tensile. In the case of a system of the multiple microdefects, the evolution problem becomes more complicated because of the existence of the effects of interaction among the microdefects. The interaction effects will be discussed in the next section.

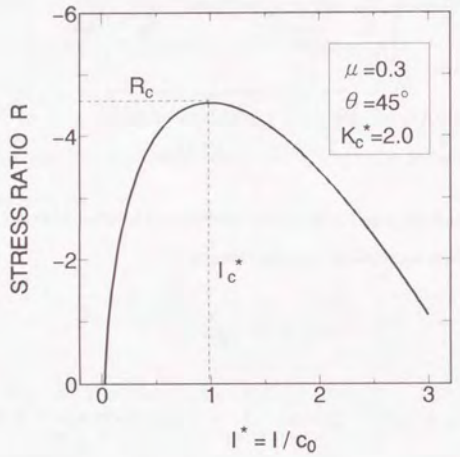

Figure 3.5 Evolution of a single microdefect under tensile confining pressure ($\sigma_2^\infty > 0$).

3.3 Interaction Effects of Discrete Microdefects

As mentioned in the previous chapter, the present theory is based on the homogenization of the method of pseudotraction. Before the interaction field and its governing equation are introduced, we begin with the method of pseudotraction for the considered model. Consider an infinite plane with two microdefects defined in the previous section; see Fig. 3.1(b). We decompose the original problem into a homogeneous problem with no microdefects and various subproblems each containing single microdefect; see Fig. 3.6(b),(c),(d).

In the present analysis, we employ the complex stress functions Φ and Ψ of Muskhelishvili [1953]. The stresses and displacements are given by

$$\begin{aligned} \sigma_{xx}(z) + \sigma_{yy}(z) &= 2\{\Phi'(z) + \overline{\Phi'(z)}\}, \\ \sigma_{yy}(z) - \sigma_{xx}(z) + 2i\sigma_{xy}(z) &= 2\{\overline{z}\Phi''(z) + \Psi'(z)\}, \\ 2G\{u_x(z) + iu_y(z)\} &= \kappa\Phi(z) - z\overline{\Phi'(z)} - \overline{\Psi(z)}, \end{aligned} \qquad \cdots\cdots (3.12)$$

where $z = x + iy$, $i = \sqrt{-1}$, G is the shear modulus and $\kappa = 3 - 4\nu$ for plane strain and $\kappa = (3-\nu)/(1+\nu)$ for plane stress, (ν being Poisson's ratio), the overbar denotes complex conjugate and prime stands for differentiation with respect to the argument.

In the subproblem α, the stress functions with respect to the local coordinate $z_\alpha = x_\alpha + iy_\alpha$ are given by

$$\begin{aligned} \Phi'_\alpha(z_\alpha) &= -\frac{1}{2\pi i\sqrt{z_\alpha^2 - l_\alpha^2}} \int_{-l_\alpha}^{l_\alpha} \frac{\sqrt{t^2 - l_\alpha^2}}{t - z_\alpha} \cdot \\ &\quad \{(\sigma_{yy}^{\infty\alpha} + \sigma_{yy}^{P\alpha}) - i(\sigma_{xy}^{\infty\alpha} + \sigma_{xy}^{P\alpha}) \\ &\quad - c_0[\lambda_1(\sigma_x^{\infty\alpha} + \sigma_{xx}^{P\alpha}) - \lambda_2(\sigma_{yy}^{\infty\alpha} + \sigma_{yy}^{P\alpha})]\delta(t)\}dt, \qquad \cdots\cdots (3.13) \\ \Psi'_\alpha(z_\alpha) &= \overline{\Phi'_\alpha(\overline{z_\alpha})} - \Phi'_\alpha(z_\alpha) - z_\alpha\Phi''_\alpha(z_\alpha), \qquad \cdots\cdots (3.14) \end{aligned}$$

where $\delta(t)$ is the Dirac delta function and the quantities $\sigma_{xx}^{P\alpha}$, $\sigma_{yy}^{P\alpha}$ and $\sigma_{xy}^{P\alpha}$ are "pseudo-

tractions", which are unknown functions to be determined as explained in the previous section.

The boundary condition of the original problem leads to the consistency equations

$$\sigma_{yy}^{P\beta} - i\sigma_{xy}^{P\beta} = \Phi'_\alpha(z_\alpha) + \overline{\Phi'_\alpha(z_\alpha)} + z_\alpha\overline{\Phi''_\alpha(z_\alpha)} + \overline{\Psi'_\alpha(z_\alpha)}, \quad \cdots\cdots (3.15)$$

$$\sigma_{xx}^{P\beta} + \sigma_{yy}^{P\beta} = 2\{\Phi'_\alpha(z_\alpha) + \overline{\Phi'_\alpha(z_\alpha)}\}, \quad \cdots\cdots (3.16)$$

where $z_\alpha = d\exp(i\phi_{\beta\alpha}) + x_\beta, (|x_\beta/l_\beta| \leq 1)$; and $d, \phi_{\beta\alpha}$ and x_β are defined in Fig. 3.6 . Equations (3.15) and (3.16) form a system of integral equations for the pseudotractions.

It is not possible to solve these integral equations in a closed form. To make the problem tractable, we assume the pseudotractions to be constant on the crack surface and $|l_\alpha/z_\alpha| \ll 1$. Neglecting higher-order terms of (l_α/z_α), the complex stress functions for the subproblem α are obtained as

$$\begin{aligned}\Phi'_\alpha(z_\alpha) &= \frac{1}{4}(\frac{l_\alpha}{z_\alpha})^2\{(\sigma_{yy}^{\infty\alpha} + \sigma_{yy}^{P\alpha}) - i(\sigma_{xy}^{\infty\alpha} + \sigma_{xy}^{P\alpha}) \\ &\quad -\frac{2c_0}{\pi l_\alpha}[\lambda_1(\sigma_{xx}^{\infty\alpha} + \sigma_{xx}^{P\alpha}) - \lambda_2(\sigma_{yy}^{\infty\alpha} + \sigma_{yy}^{P\alpha})]\}, \quad \cdots\cdots (3.17)\\ \Psi'_\alpha(z_\alpha) &= \frac{1}{2}(\frac{l_\alpha}{z_\alpha})^2\{(\sigma_{yy}^{\infty\alpha} + \sigma_{yy}^{P\alpha}) \\ &\quad -\frac{2c_0}{\pi l_\alpha}[\lambda_1(\sigma_{xx}^{\infty\alpha} + \sigma_{xx}^{P\alpha}) - \lambda_2(\sigma_{yy}^{\infty\alpha} + \sigma_{yy}^{P\alpha})]\}. \quad \cdots\cdots (3.18)\end{aligned}$$

Substituting equations (3.17), (3.18) into equations (3.15), (3.16), the consistency equations are reduced to the following expression in the global coordinate (x_1, x_2):

$$\boldsymbol{\sigma}^{P\alpha} = \boldsymbol{\gamma}^{\alpha\beta}(\boldsymbol{\sigma}^{\infty\beta} + \boldsymbol{\sigma}^{P\beta}), \quad (\beta \text{ not summed}), \cdots\cdots (3.19)$$

where $\boldsymbol{\sigma}^{\infty\alpha} = \{\sigma_{11}^{\infty\alpha}, \sigma_{22}^{\infty\alpha}, \sigma_{12}^{\infty\alpha}\}^T, \boldsymbol{\sigma}^{P\alpha} = \{\sigma_{11}^{P\alpha}, \sigma_{22}^{P\alpha}, \sigma_{12}^{P\alpha}\}^T$ and

$$[\gamma_{ij}^{\alpha\beta}] = \frac{1}{2}\left(\frac{l_\beta}{d}\right)^2 \begin{bmatrix} (1+\lambda_2 b/l_\beta)a_1 & -(\lambda_1 b/l_\beta)a_1 & a_4 \\ (1+\lambda_2 b/l_\beta)a_2 & -(\lambda_1 b/l_\beta)a_2 & a_5 \\ (1+\lambda_2 b/l_\beta)a_3 & -(\lambda_1 b/l_\beta)a_3 & a_6 \end{bmatrix} \quad \cdots\cdots (3.20)$$

with

$$\begin{aligned} a_1 &= 2\cos 2\phi_{\alpha\beta} - \cos 4\phi_{\alpha\beta}, \\ a_2 &= a_6 = \cos 4\phi_{\alpha\beta}, \\ a_3 &= a_4 = \sin 2\phi_{\alpha\beta} - \sin 4\phi_{\alpha\beta}, \\ a_5 &= \sin 2\phi_{\alpha\beta} + \sin 4\phi_{\alpha\beta}, \\ b &= 2c_0/\pi. \end{aligned}$$

The constant pseudotractions are obtained from equation (3.19). Then, the complete solution of the problem is obtained from equations (3.13),(3.14) and (3.17). The mode I stress intensity factor at the tips of the crack α is given by

$$K_I^\alpha = \sqrt{\pi l_\alpha}(\sigma_{11}^{\infty\alpha} + \sigma_{11}^{P\alpha}) + \frac{c_0}{\sqrt{\pi l_\alpha}}(-\lambda_1(\sigma_{22}^{\infty\alpha} + \sigma_{22}^{P\alpha}) + \lambda_2(\sigma_{11}^{\infty\alpha} + \sigma_{11}^{P\alpha})). \cdots (3.21)$$

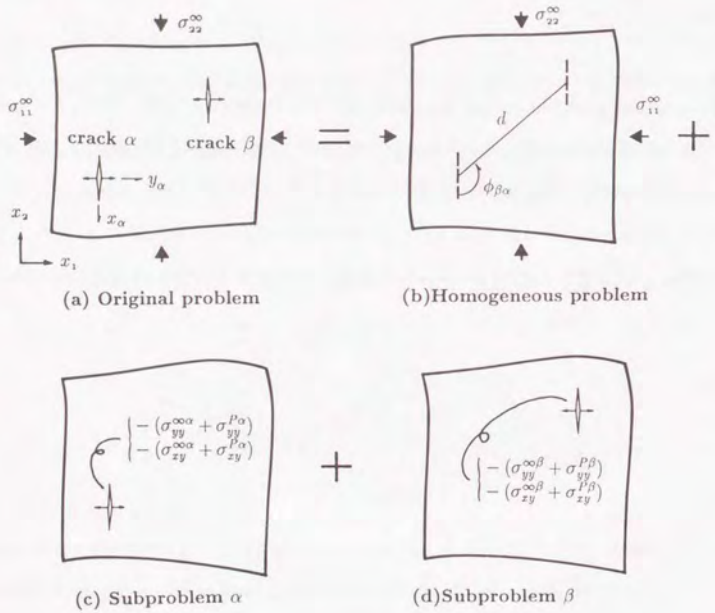

Figure 3.6 Decomposition of an original problem.

3.4 Homogenization and Governing Equations

In this subsection we carry out the homogenization, and generalize the formulation for the discrete system shown above by considering the distributed microdefects. We consider a continuous medium which contains distributed microdefects. For simplicity we consider no body force. The physical quantities for the description of mechanical behaviors are the stress and strain tensors $\hat{\sigma}$ and $\hat{\epsilon}$ and the displacement vector $\hat{u}$, which are understood as the averaged quantities over a representative volume element V_e; see Fig 3.7. Similarly to ordinary continuum theory, they satisfy the following governing equations:

[a) **Equilibrium**]

$$\nabla \cdot \hat{\sigma} = 0, \quad (3.22)$$

[b) **Strain–displacement relationship**]

$$\hat{\varepsilon} = \frac{1}{2}(\nabla \otimes \hat{u} + (\nabla \otimes \hat{u})^T), \quad (3.23)$$

where "$\cdot$" and "$\otimes$" denote the first order contraction and tensor product respectively, and ∇ is defined by $(\nabla)_i \equiv \partial/\partial x_i$.

The constitutive equation consists of the stress–strain relationship for a certain state of microdefects and the evolution law of the microdefects. The former relationship is given by the one between the average stress $\hat{\sigma}$ and the average strain $\hat{\epsilon}$ of the elastic solid containing many microdefects. Horii and Nemat-Nasser [1983] derived the following relationship:

[c) **Stress-strain relationship**]

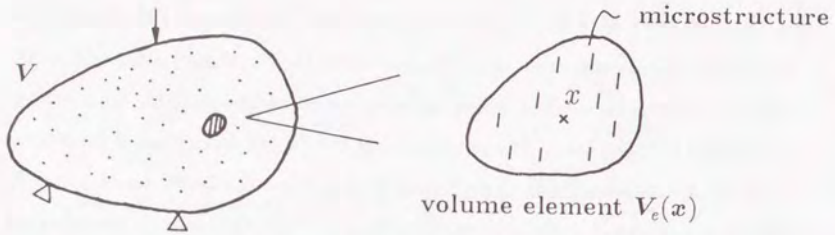

Figure 3.7 Representative volume element.

$$\hat{\sigma} = \boldsymbol{D}^e : (\hat{\varepsilon} - \hat{\varepsilon}^*), \quad (3.24)$$

$$\hat{\varepsilon}^* = \frac{1}{V_e}\int_S \frac{1}{2}([u] \otimes n + n \otimes [u])ds, \quad (3.25)$$

where $\boldsymbol{D}^e$ is the elastic moduli of the matrix, and $\hat{\varepsilon}^*$ is the average strain due to the displacement gap $[u] \equiv u^+ - u^-$ along the microdefect surface with unit normal vector n, S being the surfaces of microdefects contained in the representative volume V_e.

If the displacement gap $[u]$ is expressed in terms of the average stress by solving the problem of many microdefects, the strain due to the displacement gap is given by

$$\hat{\varepsilon}^* = \boldsymbol{C}^* : \hat{\sigma}. \quad (3.26)$$

Substituting equation (3.24) into equation (3.26), we have

$$\hat{\varepsilon}^* = \boldsymbol{H} : \hat{\varepsilon}, \quad (3.27)$$

where

$$\boldsymbol{H} = (\boldsymbol{I} + \boldsymbol{C}^* : \boldsymbol{D}^e)^{-1} : \boldsymbol{C}^* : \boldsymbol{D}^e, \quad (3.28)$$

where $\boldsymbol{I}$ is the fourth-order identity tensor. The expression of $\boldsymbol{H}$ becomes simple for the present case as shown later.

Substituting equation (3.27) into equation (3.24), the stress-strain relationship is given by

$$\hat{\sigma} = \boldsymbol{D}^e : (\boldsymbol{I} - \boldsymbol{H}) : \hat{\varepsilon}. \quad (3.29)$$

For the present two-dimensional problem, we set $\hat{\sigma} = \{\hat{\sigma}_{11}, \hat{\sigma}_{22}, \hat{\sigma}_{12}\}^T$ and $\hat{\epsilon} = \{\hat{\varepsilon}_{11}, \hat{\varepsilon}_{22}, 2\hat{\varepsilon}_{12}\}^T$. Thus, the tensors $\boldsymbol{C}^*, \boldsymbol{D}^e, \boldsymbol{I}$ and $\boldsymbol{H}$ are reduced to 3×3 matrices, and the elastic moduli $\boldsymbol{D}^e$ are given by

$$[D^e_{ij}] = \frac{E}{(1+\nu)(1-2\nu)} \begin{bmatrix} 1-\nu & \nu & 0 \\ \nu & 1-\nu & 0 \\ 0 & 0 & (1-2\nu)/2 \end{bmatrix} \quad (3.30)$$

for plane strain and

$$[D^e_{ij}] = \frac{E}{1-\nu^2} \begin{bmatrix} 1 & \nu & 0 \\ \nu & 1 & 0 \\ 0 & 0 & (1-\nu)/2 \end{bmatrix} \quad (3.31)$$

for plane stress; E being Young's modulus.

In general, it is difficult to obtain an explicit expression of the matrix $\boldsymbol{C}^*$ and accordingly $\boldsymbol{H}$, since it requires the displacement gap $[u]$ in the problem of many

microdefects; see equations (3.25)–(3.27). However, neglecting the effects of interaction among microdefects, matrix $\boldsymbol{H}$ is given by

$$H_{ii} = \frac{2\rho l\{(\pi l + 2\lambda_2 c_0)D^e_{ii} + 2\lambda_1 c_0 D^e_{2i}\}}{E' + 2\rho l\{(\pi l + 2\lambda_2 c_0)D^e_{11} + 2\lambda_1 c_0 D^e_{21}\}}, \qquad (i = 1, 2),$$
$$H_{33} = \frac{2\rho l^2 \pi D^e_{33}}{E' + 2\rho l^2 \pi D^e_{33}}, \qquad \text{otherwise } H_{ij} = 0, \qquad \cdots\cdots (3.32)$$

where ρ is the crack density (the number of microdefects per unit area) and $E' = E$ for plane stress and $E' = E/(1-\nu^2)$ for plane strain. Note that the microdefects are distributed over the domain, and the half crack length l and crack density ρ are continuous field variables.

The damage evolution in the present case is the increase in the crack length l with a constant crack density ρ. Hence, the crack length serves as the damage parameter. We employ linear elastic fracture mechanics for the crack extensions. For generality of the formulation, we express the Griffith's criterion with a damage surface f as

$$f = K_I - K_c, \cdots\cdots (3.33)$$

where K_c is a fracture toughness. Then, the evolution law is described as follows:

[d) **Evolution law**]

$$\begin{cases} f > 0 \ ; & \text{(not admissible)} \\ f = 0 \ ; \ \delta l \geq 0 & \text{(possible growth)} \\ f < 0 \ ; \ \delta l = 0 & \text{(no growth).} \end{cases} \cdots\cdots (3.34)$$

As discussed before, evaluation of the interaction effects in the evolution law is the key point in the theory. To take account of the direct effects of interaction, we apply and extend the method of pseudotraction for distributed microdefects.

For the discrete system, the pseudotractions are defined for each microdefect. For distributed microdefects, we introduce a tensor field named the interaction field which is an extension of the pseudotraction. As is the case with the discrete system, we consider the decomposition of the problem. In examining the evolution of microdefects at a particular point, we consider a single microdefect located at that point. The number of other microdefects is not finite, but they are located over the domain with a certain distribution of crack density $\rho(\boldsymbol{x})$ and crack length $l(\boldsymbol{x})$. Hence the number of other subproblems is understood to be infinite; see Fig. 3.6. In the subproblem with the microdefect under consideration, we apply pseudotraction calculated from the interaction field on the surface of the microdefect. (The relation between the pseudotraction and the interaction field is the same as that of the traction vector and the stress tensor. In the present situation, the component of the interaction field is that of the pseudotraction.) Then, the mode I stress intensity factor of the microdefect is given by

$$K_I = \sqrt{\pi l}(\hat{\sigma}_{11} + \sigma^P_{11}) + \frac{c_0}{\sqrt{\pi l}}(-\lambda_1(\hat{\sigma}_{22} + \sigma^P_{22}) + \lambda_2(\hat{\sigma}_{11} + \sigma^P_{11})). \cdots\cdots (3.35)$$

Hence, the damage surface is given by

$$f(\hat{\boldsymbol{\sigma}}, \boldsymbol{\sigma}^P, l) = \sqrt{\pi l}(\hat{\sigma}_{11} + \sigma^P_{11}) + \frac{c_0}{\sqrt{\pi l}}(-\lambda_1(\hat{\sigma}_{22} + \sigma^P_{22}) + \lambda_2(\hat{\sigma}_{11} + \sigma^P_{11})) - K_c. \quad (3.36)$$

Note that $\hat{\boldsymbol{\sigma}}$, $\boldsymbol{\sigma}^P$, l are all field variables and this evolution law is satisfied at all points in the domain.

Since the distributed microdefects are considered and the number of the subproblems is infinite, the consistency condition, which ensures the traction-free condition of the surface, takes the following form :

[e) **Consistency equation**]

$$\sigma^P(\boldsymbol{x}) = \int_V \rho\gamma(\boldsymbol{x} \mid \boldsymbol{\xi})\{\hat{\sigma}(\boldsymbol{\xi}) + \sigma^P(\boldsymbol{\xi})\}d\boldsymbol{\xi}, \quad \cdots\cdots\cdots\cdots\cdots\cdots\cdots\cdots\cdots\cdots \quad (3.37)$$

where $\gamma(\boldsymbol{x} \mid \boldsymbol{\xi})$ is the same definition of $\gamma_{ij}^{\alpha\beta}$ as in equation (3.20), except $d = \| \boldsymbol{x} - \boldsymbol{\xi} \|$ and l_β and $\phi_{\beta\alpha}$ are replaced by the half crack length at the point $\boldsymbol{\xi}$: $l(\boldsymbol{\xi})$ and $\phi = \tan^{-1}(x_2 - \xi_2)/(x_1 - \xi_1) + \pi/2$, respectively.

3.5 Comparison with CDM

To illustrate the features of the proposed theory, we present the conventional CDM for the same problem and make a comparison with them. In CDM, the direct interaction effects among microdefects are not taken into account, and a single microdefect in an infinite body is considered. When the evolution of a microdefect at a particular point is investigated, the stress at that point is applied on the infinite solid with a single microdefect at infinity. Then the damage surface becomes

$$f(\hat{\boldsymbol{\sigma}}, l) = \sqrt{\pi l}\hat{\sigma}_{11} + \frac{c_0}{\sqrt{\pi l}}(-\lambda_1\hat{\sigma}_{22} + \lambda_2\hat{\sigma}_{11}) - K_c. \quad \cdots\cdots\cdots\cdots\cdots\cdots\cdots\cdots \quad (3.38)$$

The other governing equations, the equilibrium equation, the strain–displacement relationship and the stress–strain relationship, are the same as in IFT. The governing equations and the unknowns of these theories are summarized in Table 3.1. In the next section, the numerical examples from these theories will be shown.

Note that the main feature that distinguishes IFT from CDM is the fact that the stress–strain relationship at any given point depends on the stress and crack length at all other points. In CDM, eliminating the damage parameter l from the stress–strain relationship (3.29) with the evolution law equations [(3.34) and (3.38)], the constitutive relation of CDM is obtained. Then, this constitutive relation is described by the

Table 3.1 Summary of governing equations and unknowns

	IFT	CDM
Equilibrium	Equation (3.22)	Equation (3.22)
ε–u relation	Equation (3.23)	Equation (3.23)
σ–ε relation	Equation (3.29)	Equation (3.29)
Evolution law	Equations (3.34) and (3.36)	Equations (3.34) and (3.38)
Consistency eq.	Equation (3.37)	—
Unknowns	$\hat{\boldsymbol{u}}, \hat{\boldsymbol{\epsilon}}, \hat{\boldsymbol{\sigma}}$, $l, \boldsymbol{\sigma}^P$	$\hat{\boldsymbol{u}}, \hat{\boldsymbol{\epsilon}}, \hat{\boldsymbol{\sigma}}$, l

(IFT : Interaction Field Theory)

local stress at the considered point. On the other hand, in IFT, if we substitute equation (3.37) into equation (3.36), the damage parameter $l(\boldsymbol{x})$ is obtained as a function of the stress $\boldsymbol{\sigma}(\boldsymbol{x}')$ at all other points $\boldsymbol{x}'$. Since $\boldsymbol{H}$, obtained from equation (3.32), is a function of the damage parameter $l(\boldsymbol{x})$, the stress–strain relationship (3.29) depends on the stress at all points in the body. Since the behavior of the material depends on the stress at other points, the derived constitutive equation is understood as nonlocal. Such a nonlocal constitutive relation due to long–range effects is also discussed by Eringen and Edlen [1972].

3.6 Numerical Results and Discussion

Before presenting the numerical results, we report a brief description of the finite element discretization. We employ the conventional three–node triangular element

for the approximation of the displacement field $\hat{u}$. The damage parameter l and the interaction field σ^P are approximated to be constant in an element. Employing the principle of virtual work, $2N$ discretized equilibrium equations are obtained, in which N is the total number of nodal points and the stiffness matrix is a nonlinear function of the damage parameter l. To simplify the numerical calculations, the evolution law (3.34) is approximated by $f = 0$. This corresponds to making the irreversible variable l reversible, and hence to reducing the inelastic problem to the nonlinear elastic problem. Then, the evolution law $f = 0$ with the damage surface (3.36) is discretized to be M algebraic equations; and evaluating the integral in equation (3.37) numerically, the consistency equation is also reduced to $3M$ nonlinear algebraic equations, where M is the total number of elements. Thus, we have a system of $2N + 4M$ nonlinear equations for $2N + 4M$ unknowns, $2N$ nodal displacements, a $3M$-element interaction field and an M-element damage parameter. In the case of CDM, from equations (3.22),(3.23) and (3.29) and the evolution law $f = 0$ with the damage surface of CDM [equation (3.38)] , a system of $2N + M$ nonlinear algebraic equations is obtained, consisting of $2N$ discretized equilibrium equations and M evolution equations. These systems of nonlinear algebraic equations are solved by Newton's method.

3.6.1 Comparison between CDM and IFT

The main purpose of the numerical calculations in this subsection is to investigate whether these theories can simulate localization phenomena. Thus, we restrict our attention to simple numerical examples. We consider a biaxial test of a rock block under a plane strain condition; see Fig. 3.8. The dimensions of the rock block are $200c_0 \times 200c_0$, where c_0 is half the length of the initial defect. The numbers in Fig. 3.8 denote the element numbers of the finite model. Both the top and bottom boundaries of the rock block are assumed to be smooth surfaces (laterally sliding). The following

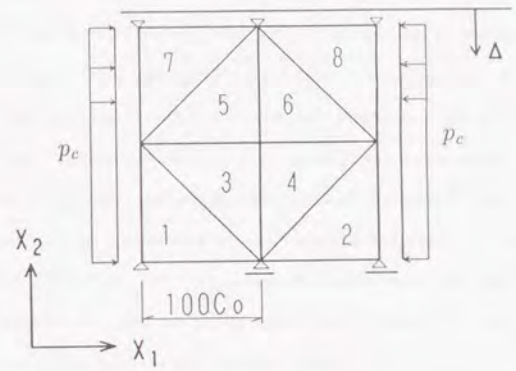

Figure 3.8 Finite element mesh of biaxial test of rock block.

values are used in all calculations: normalized Young's modulus $E/\sigma_0 = 1000$, Poisson's ratio $\nu = 0.3$ and the normalized crack density $\rho c_0^2 = 0.3$, where σ_0 is the reference stress defined by $\sigma_0 = K_c/\sqrt{\pi c_0}$ with the fracture toughness of the material K_c. In addition, when we set the frictional coefficient of the initial defect $\mu = 0.3$ and the angle of the initial defect $\theta = \pi/4$, then $\lambda_i \quad (i = 1, 2)$ in equation (3.3) are 0.49 and 0.92, respectively. At initial loading stages, the block is loaded both in the horizontal and vertical directions. The vertical loading is implemented by prescribing the same increments of vertical displacements of all nodal points at the top of the block. After the horizontal loading reaches a specific normalized confining pressure p_c/σ_0, only the vertical displacements are incremented.

Tensile confining pressure

In the first place, the numerical calculations are carried out for the case of the normalized confining pressure $p_c/\sigma_0 = 0.2$ (positive tension). Figure 3.9 shows the relations

between the normalized axial stress $\hat{\sigma}_{22}/\sigma_0$ and the normalized damage parameter (crack length) in element 4 calculated by IFT and CDM. With increasing the normalized axial stress, the damage parameters calculated by using both theories evolve, and the axial stresses reach their maximum values. Even in the descending part of the axial stress, the damage parameters are increasing. This behavior means that the damage evolves unstably, if the specimen is loaded with the load control method, and is called damage softening to be distinguished from the strain softening in the stress–strain relation. Since these behaviors are almost similar to those of the evolution of the single microdefect discussed in section 3.2, the cause of the damage softening is interpreted as not the interaction effects but the nature of the microdefect model. However the damage parameter of IFT is suppressed because of the interaction effects, and is about one fourth of the damage parameter of CDM at each of the maximum axial stresses.

Since the stress–strain relation of these theories [equation (3.29)] depends on the damage parameter, the fact that the damage parameters evolve with decreasing the normalized axial stress means the strain softening behavior in the stress–strain relation. It is well known that the strain softening in the constitutive relation promotes localization of damage or deformation. The fact that localization behavior due to damage softening has taken place is shown by the numerical simulation of these theories. Figure 3.10 shows the distributions of the damage parameters in the post-peak regime and the radii of the circles denote the magnitudes of the damage parameters. In both theories, the damage localizes into the vertical direction.

Compressive confining Pressure

Figure 3.11 shows the evolution of the crack lengths (damage parameters) in every element with the normalized confining pressure $p_c/\sigma_0 = -2.0$ for the cases of both IFT and CDM. At the initial loading stage, all crack lengths of IFT as well as CDM grow

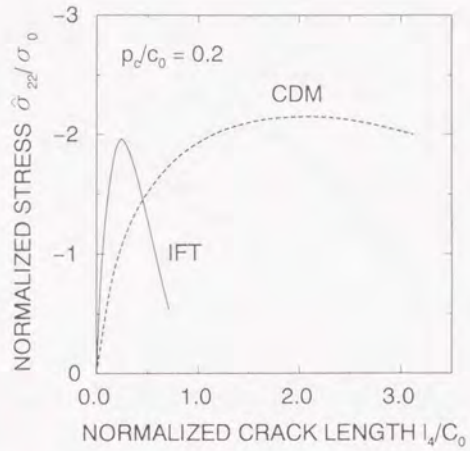

Figure 3.9 Axial stress vs crack length (damage parameter) curve with normalized confining pressure $p_c/\sigma_0 = 0.2$. Comparison between IFT and CDM.

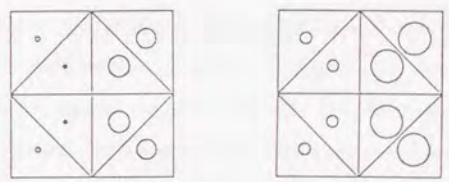

Figure 3.10 Distribution of crack length (damage parameter) in post-peak regime with normalized confining pressure $p_c/\sigma_0 = 0.2$: (a) IFT at $\hat{\sigma}_{22}/\sigma_0 = -1.59$; (b) CDM at $\hat{\sigma}_{22}/\sigma_0 = -2.00$.

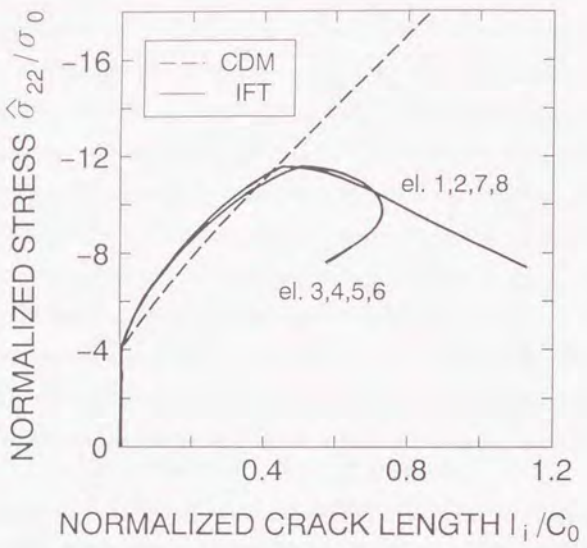

Figure 3.11 Axial stress vs crack length (damage parameter) curve with normalized confining pressure $p_c/\sigma_0 = -2.0$. Comparison between IFT and CDM.

uniformly; however, the damage evolution (crack growth) of IFT is relatively restrained by the interaction effect. As the external load is increased further, the damage evolution in IFT is more accelerated. After the critical load is attained, all damage parameters still increase with the decreasing load (damage softening). Moreover, the distribution of the damage gradually loses its uniformity in the specimen. In contrast to IFT, all damage parameters in CDM are identical in the specimen at all loading stages, and there is no critical load.

To detect bifurcation points, an eigenvalue analysis of the linearized operator of the nonlinear equations is carried out at each incremental step. The solution of CDM has no bifurcating paths since no negative eigenvalues are calculated for the linearized

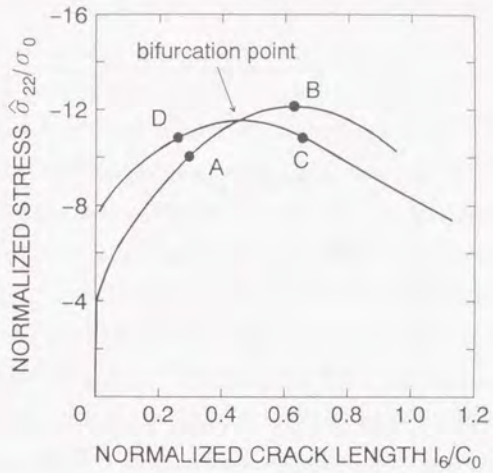

Figure 3.12 Evolution of damage parameter in element 6 for IFT. Fundamental path (path A to B) and bifurcating path (path C to D).

operator of CDM. Contrary to the solution of CDM, the eigenvalue analysis for IFT shows that almost zero or negative eigenvalues exist, and consequently the solution of IFT is found to contain the possibility of bifurcation. After a bifurcation point is identified, the bifurcation paths are traced employing the switching procedure [Keller, 1977]. In Fig. 3.12, the bifurcation path (path C to D) as well as the fundamental path (path A to B) are plotted for the damage parameter of element 6. It is found that the load at the bifurcation point is lower than the maximum load along the fundamental path, and that the damage softening behavior along both bifurcating paths is presented. This implies that, if the specimen is loaded with the load control method, the damage evolution becomes unstable at the bifurcation point.

Figure 3.13 shows (a) the relation between the damage parameter of element 3 and that of element 4 and (b) the distribution of the damage parameters corresponding

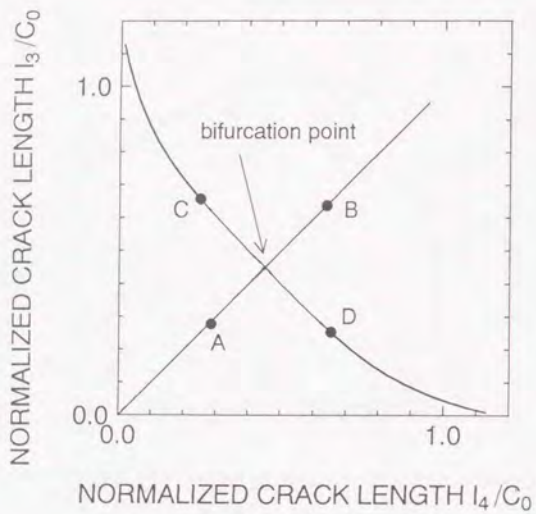

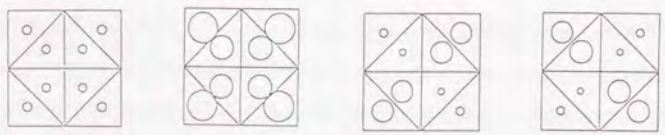

(b)

Figure 3.13 (a) Crack length (damage parameter) in element 3 vs that in element 4. (b) Distribution of damage parameter at point A–D with normalized confining pressure $p_c/\sigma_0 = -2.0$.

to the points A–D in Fig. 3.12. In Fig. 3.13 (b), the radii of the circles denote the magnitude of the damage parameters. The damage parameters of element 3 and 4 on the fundamental path are identical; the symmetry of the distribution of the damage parameters is preserved even on the path after the bifurcation point. On the other hand, on the bifurcating path the damage parameters of the elements in the diagonal direction increase and the others decrease with the decreasing load. In addition, the distributions of the damage parameters at points C and D are antisymmetric to each other. The symmetrical breaking due to bifurcation is often found in nonlinear problems such as buckling of shells [Fujii and Yamaguti, 1980], fluid mechanics and biomathematics. For the present problem, this shows the features observed in the localization of damage or the shear band formation in laboratory tests of rock specimen. It is confirmed that IFT can simulate these localization phenomena as well as damage softening, while conventional CDM cannot reproduce those features.

3.6.2 Effects of Confining Pressure

As another numerical example, we examine the effect of confining pressure on the solution of IFT. Figure 3.14 shows the mesh configuration used in the following numerical calculation and the damage evolution of element 8 with different normalized confining pressures p_c/σ_0. All the material parameters and the boundary condition are the same as the preceding numerical example except the specific normalized confining pressure. We choose the bifurcating path on which the damage parameter in element 8 is extended. With increasing confining pressure, the critical (bifurcation) load increases and the evolution of the damage is suppressed. In Figs 3.15 and 3.16, we show typical deformation characteristics in a biaxial test. Figure 3.15 shows the stress–strain curves of element 8 for the normalized confining pressures $p_c/\sigma_0 = -2.0, -1.0$ and -0.05. The relations between the normalized stress difference $(\hat{\sigma}_2 - \hat{\sigma}_1)/\sigma_0$ and the overall

volumetric strain $\Delta V/V$ are shown in Fig. 3.16. In postcritical load, the dilation is increased with the decreasing confining pressure. These features agree with experimental observations [Brace et al., 1966; Zoback and Byerlee, 1975; Gowd and Rummel, 1980].

It is worth noting that, with decrease in the confining pressure, a different pattern of the distribution of the damage parameters occurs. When $p_c/\sigma_0 < -0.08$, the localization of the damage parameters occurs along the vertical direction. To illustrate this situation, we also plot the distribution of the damage parameters with the different normalized confining pressures in the post bifurcation regime in Fig. 3.17. Figure 3.17(c) indicates the axial splitting mode, which is observed in laboratory tests with very low confining pressure or uniaxial compression. It is shown that IFT reproduces the axial splitting mode as well as the shear failure mode.

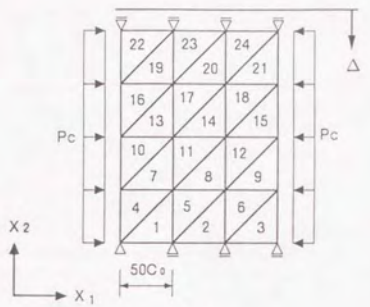

(a)

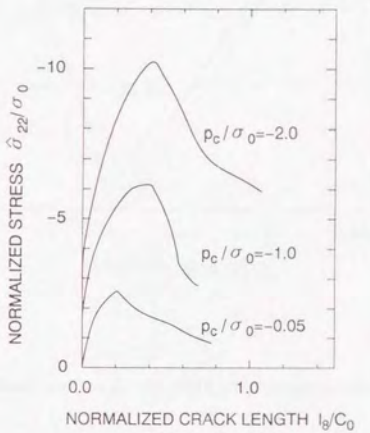

(b)

Figure 3.14 (a)Finite element mesh. (b)Effect of normalized confining pressure p_c/σ_0 on damage evolution of element 8.

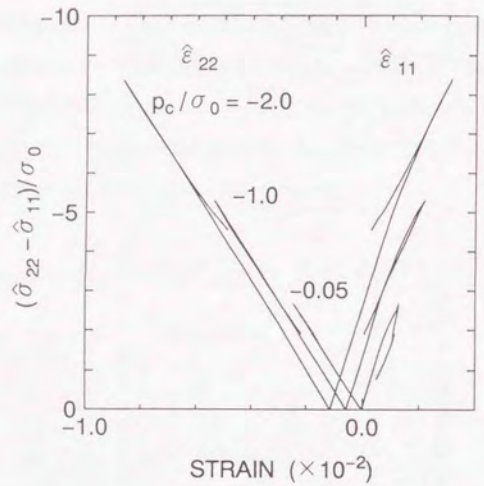

Figure 3.15 Stress–strain curves with different normalized confining pressure p_c/σ_0.

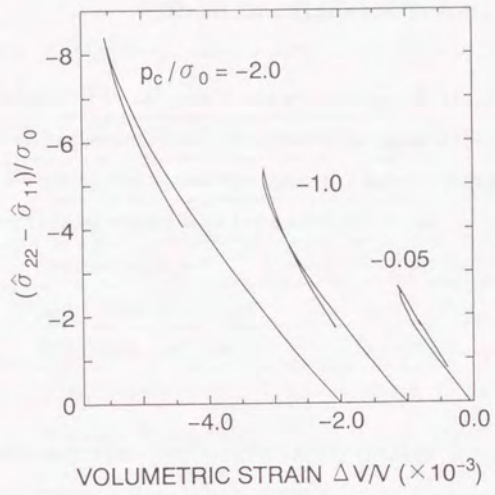

Figure 3.16 Volumetric strain vs stress difference curves with different normalized confining pressure p_c/σ_0.

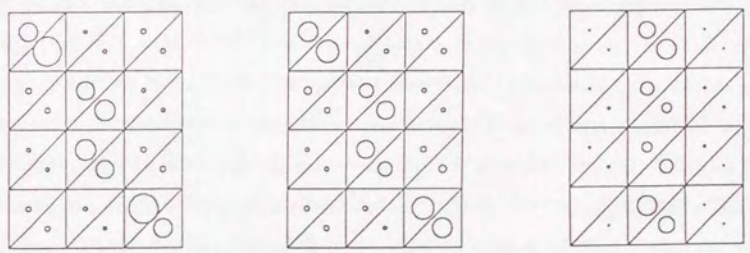

Figure 3.17 Distribution of damage parameter with different normalized confining pressure; (a) $p_c/\sigma_0 = -2.0$; (b) $p_c/\sigma_0 = -1.0$; (c) $p_c/\sigma_0 = -0.05$.

3.6.3 Prediction of Strengths of Rocks

Employing the proposed theory, the strengths of materials under compression are obtained as a function of the confining pressure. We shall compare the failure envelopes of actual rocks obtained by uniaxial or triaxial experiments with numerical results which is evaluated as the envelope of the bifurcating axial stresses under various confining pressures.

Granite

As the first illustration, Westerly granite is chosen for comparison because Westerly granite is the most typical brittle rock for mechanical testing. From earlier studies, the mechanical characteristics of Westerly granite is well known; the grain size is 750 μm; and the pore porosity is 0.7 % [Brace, 1965]. The experimental strengths reported by Brace et al. [1966] and Mogi [1966] are used in the following comparison.

The parameters used in the present simulations are listed in Table 3.2. The Young's modulus and Poisson ratio are evaluated to be $E = 5.7 \times 10^4$ MPa, $\nu = 0.32$, based on the data of the uniaxial compression test reported by Brace et al. [1966]. Since these material constants are defined as those of the elastic matrix (without influence of microdefects), the constants are evaluated from the data in the linear part of the stress–strain diagram of the uniaxial test. Because the reported fracture toughness K_c for Westerly granite is of the order $0.60 \sim 2.50$ MPam$^{1/2}$ [Atkinson, 1987], we choose the fracture toughness $K_c = 1.0$ MPam$^{1/2}$. Hadley [1975] reports crack density and averaged crack length of unstressed and stressed samples of Westerly granite with the scanning electron microscope. According to his observation, the average crack length and the nondimensional crack density of unstressed Westerly granite are 17.7 μm and 0.18, respectively. We use half the length of the initial defect $c_0 = 17.7/2 = 9\mu$m,

Table 3.2 Model parameters used in numerical calculation for Westerly granite

Parameter	Value
Young's modulus	$E = 5.7 \times 10^4$ MPa
Poisson's ratio	$\nu = 0.32$
Fracture toughness	$K_c = 1.0$ MPam$^{1/2}$
Initial defect length	$c_0 = 9$ μm
Normalized crack density	$\rho c_0^2 = 0.32$
Angle between initial defect and loading axis	$\theta = 30,\ 40,\ 45,\ 50,\ 60$ deg
Coefficient of friction	$\mu = 0.2,\ 0.3,\ 0.4$

and accordingly the reference stress becomes $\sigma_0 = K_c/\sqrt{\pi c_0} = 266$ MPa. The theory presented in this paper is a two-dimensional one, while the experimental results are obtained from cylindrical samples. Thus, a certain amount of adjustment in the model parameters is required. As the two-dimensional crack density, we use $\rho c_0^2 = (0.18)^{2/3} = 0.32$.

As for the other parameters, it is necessary to determine the orientation of the initial defects and the coefficient of friction. According to the data reported by Sprunt and Brace [1974], the orientation of the initial defects in unstressed samples of Westerly granite is distributed homogeneously and has no preferred direction. Thus, even in the numerical calculations, the statistically homogeneous distribution of the orientation angle should be considered. However, the tension cracks start to nucleate at the tips of the initial defects which are most likely to slide with the increase in loading, and these tension cracks seem to govern the macroscopic failure. In the following, thus, the numerical calculations are carried out for the several values of the orientation angle

instead of the case of the homogeneous distribution of the orientation angle.

On the other hand, the coefficient of the friction used in this simulation should be interpreted as, in actual rocks, that on grain boundaries between similar materials or a mica and any other grain. It is difficult to obtain plausible value of the frictional coefficient. Thus, after the effect of the orientation angle on the failure envelope is examined, the effect of the frictional coefficient is illustrated for the specific angle of the orientation.

Figure 3.18 illustrates the effect of the orientation angle θ on the normalized axial strength (bifurcation stress) under various normalized confining pressures p_c/σ_0 for the frictional coefficient $\mu = 0.3$. In each case of the confining pressures, the axial strength at about $\theta = 45$ deg prescribes the minimum axial strength and this behavior accords with the fact that the concentrated force F defined by equation (3.2) becomes maximum at about $\theta = 45$ deg; see Fig. 3.2. It may be concluded that, for the whole range of the confining pressure, the axial strength and the associated macroscopic fracture are governed by the tension cracks which grow at the tips of the initial defects with an orientation angle $\theta = 45$ deg.

Figure 3.19 shows theoretical and experimental failure envelops for Westerly granite. In this numerical calculation, the orientation angle is assigned to $\theta = 45$ deg, because the minimum failure envelope is obtained for the case of this orientation angle. For the case of $\theta = 45$ deg and $\mu = 0.3$, when the confining pressure is less than about 20 MPa, axial splitting modes occur as a macroscopic fracture mode, and the strengths in this mode are governed by the maximum initial defect in the sample. In fact, Hadley reports that the maximum observed crack in the unstressed sample of Westerly granite is 565 μm in length. The solution of IFT using the averaged crack length is overestimating. On the other hand, when the confining pressure is greater than 600 MPa, the failure envelope of experimental results deviates from the solution of IFT. This deviation from

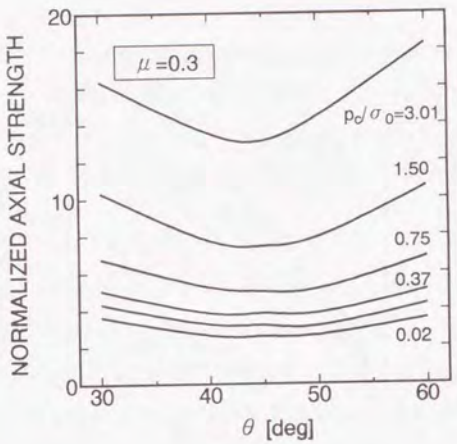

Figure 3.18 Effect of orientation angle θ of the initial defect on axial strength (bifurcation stress) under various normalized confining pressures p_c/σ_0 for the frictional coefficient $\mu = 0.3$.

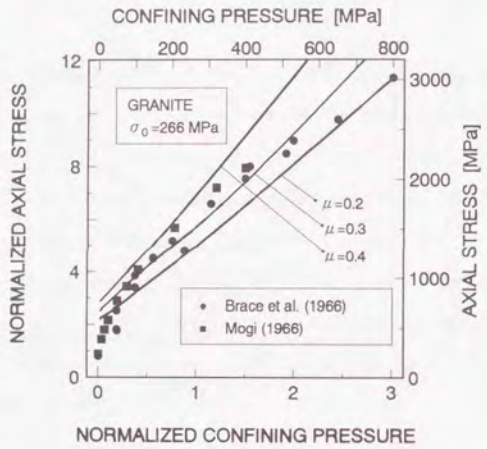

Figure 3.19 Comparison between experimental and theoretical failure envelopes for the angle of the initial defect $\theta = 45$ deg with various frictional coefficients μ.

theoretical value is interpreted as the effect of the plastic deformation of the material, which is not considered in the present theory. Nevertheless, in the range of the confining pressure from 20 MPa to 600 MPa, the fit shown in Fig. 3.19 is acceptably good.

Gabbro

Shimada et al. [1983] studied experimentally the dependence of the strength of Murotomisaki gabbro on confining pressure. Murotomisaki gabbro is silicate rock of which the grain size of the olivine component is 1–2 mm, pyroxene is about 0.7 mm and the plagioclase is about 0.7–3 mm. The apparent density 2.985 Kg/m^3 and the porosity 0.4 %.

The used model parameters are listed in Table 3.3. The Young's modulus and Poisson's ratio are evaluated from the stress–strain curve of the uniaxial test by Shimada et al., [1983]. Since the fracture toughness of Murotomisaki gabbro is not reported, the used value is determined from the reported data for other kinds of gabbro, such as 2.2–2.9 MPam$^{1/2}$ for Kallax gabbro [Ouchterlony et al., 1988] and 2.7–3.0 MPam$^{1/2}$ for Black gabbro [Atkinson and Meredith, 1987]. The half length of initial defect is determined as follows: for Westerly granite, the half length of initial defect and the mean grain size are 9 and 750 μm, respectively, while the grain size of Murotomisaki gabbro is 2000 μm; and thus the half length of Murotomisaki gabbro is $c_0 = 2000/750 \times 9 = 24$ μm. Furthermore, to make a comparison, $c_0 = 70$ μm is also used, which is about three times 24 μm. After the lengths of initial defect are fixed, the normalized density of microdefects and the frictional coefficient are assigned so that the numerical envelopes may fit the experimental data. The experimental and numerical envelopes are shown in Fig. 3.20.

Shimada et al. also reported Acoustic Emission (AE) activity during axial loading

Table 3.3 Model parameters used in numerical calculation for Murotomisaki gabbro

Parameter	Value
Young's modulus	$E = 9.0 \times 10^4$ MPa
Poisson's ratio	$\nu = 0.25$
Fracture toughness	$K_c = 2.5$ MPam$^{1/2}$
Initial defect length	$c_0 = 24,\ 70\ \mu$m
Angle between initial defect and loading axis	$\theta = 45$ deg
Normalized crack density	$\rho c_0^2 = 0.5,\ 0.7$
Coefficient of friction	$\mu = 0.2,\ 0.3$

under several confining pressures. Under low confining pressure, the AE rate began to increase at the onset of dilatancy and accelerated rapidly followed by macroscopic failure. On the other hand, under high confining pressure, no rapid increase before macroscopic failure was observed and the AE rate stayed constant. The pattern of the AE activity changed at a confining pressure between 0.51 and 0.76 GPa. This change can be interpreted as brittle–ductile transition in failure process. The range of the confining pressure at the brittle–ductile transition agrees with the confining pressure at which the theoretical envelops begin to deviate from the experimental data. Thus, the deviation for confining pressures ranging from about 0.5 GPa is due to the plastic deformation of the matrix.

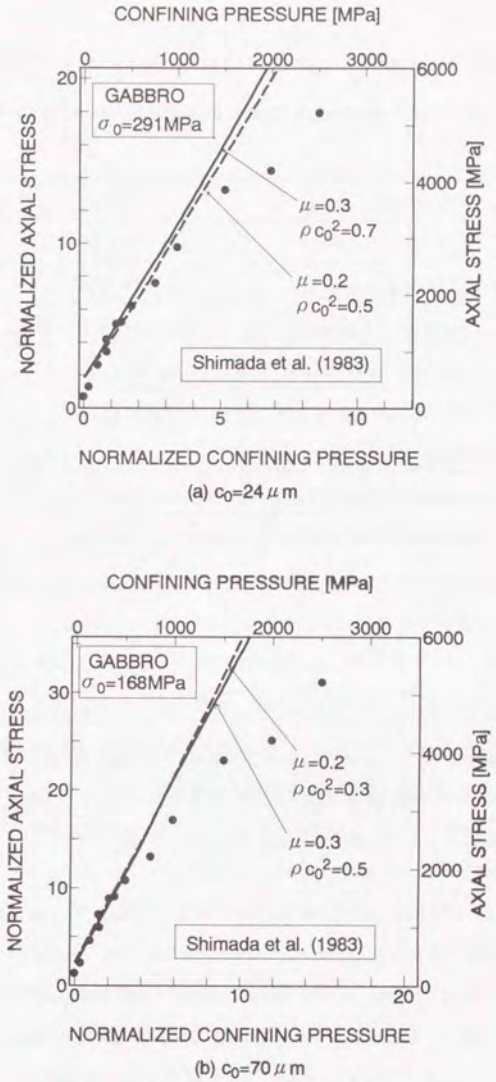

Figure 3.20 Comparison between experimental and numerical failure envelopes for Murotomisaki gabbro. (a) $c_0 = 24\mu$m; (b) $c_0 = 70\mu$m.

Table 3.4 Model parameters used in numerical calculation for limestone

Parameter	Value
Young's modulus	$E = 6.8 \times 10^4$ MPa
Poisson's ratio	$\nu = 0.30$
Fracture toughness	$K_c = 1.0$ MPam$^{1/2}$
Initial defect length	$c_0 = 7,\ 25\ \mu$m
Angle between initial defect and loading axis	$\theta = 45$ deg
Normalized crack density	$\rho c_0^2 = 0.5,\ 0.7,\ 1.2,\ 1.5$
Coefficient of friction	$\mu = 0.2,\ 0.3$

Limestone

The limestone used to compare here is made up of oölites, relatively large calcite grains and fossil fragments in a cement of finer grained carbonate material. The oölites are somewhat ellipsoidal with an average longer dimension of 0.93 mm; the calcite grains average about 0.6 mm in diameter [Donath et al., 1971].

The model parameters are shown in Table 3.4, in which Young's modulus is evaluated from the stress–strain diagram of Solenhofen limestone reported by Wawersik and Fairhurst [1969], and Poisson ratio is from Yamaguti and Nishimatu [1980]. By a similar method for gabbro, the length of the initial defect is assigned to $c_0 = 9 \times 600/750 = 7\ \mu$m and $c_0 = 25\mu$m. The reported values of fracture toughness of limestone are between 1.03 and 1.36 MPam$^{1/2}$ (Klinthagen limestone: 1.03–1.31 MPam$^{1/2}$; Irondequoit limestone: 1.36 MPam$^{1/2}$) [Atkinson and Meredith, 1987]. The other parameters are determined by fitting numerical results to the experimental strength reported by

Donath et al., [1971]. The comparison the numerical envelope and experimental one is shown in Fig. 3.21.

Marble

The experimental strengths of a marble for the comparison shown in Fig. 3.22 are from Donath et al. [1971], who reported that the samples of the marble are extracted from Beldens formation and its average grain size is from 0.5 to 0.6 mm. The model parameters used in the numerical calculations are listed in Table 3.5, in which Young's modulus is evaluated from the data for Tennessee marble reported by Wawersik and Fairhurst [1970]; Poisson ratio is from Goodman [1980]. The reported value of the fracture toughness is ranging from 0.62 to 1.49 MPam$^{1/2}$ [Atkinson and Meredith, 1987]. Figure 3.22(a) shows the comparison between the experimental and numerical envelops for the initial defect length $c_0 = 7\ \mu$m based on the ratio of the grain size in Beldens marble to that in Westerly granite. The comparison for $c_0 = 40\ \mu$m is illustrated in Fig. 3.22(b), where the agreement between the theoretical and the experimental results is better than that in Fig. 3.22(a). In addition, for the case of Fig. 3.22(a) the values of the normalized crack density, which are determined by fitting the numerical envelop to the experimental one, are unrealistically large. Thus, it seems that the actual average length of initial defects in Beldens marble is larger than the value evaluated from the ratio of the grain sizes.

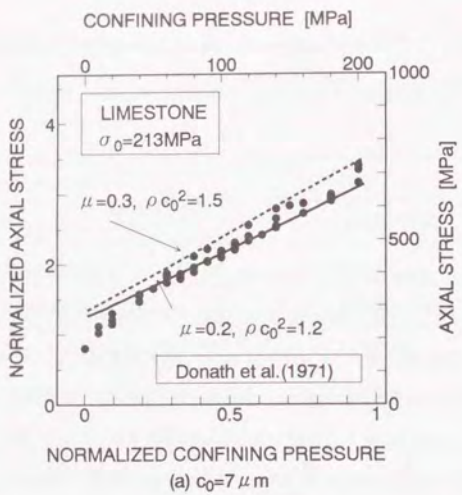

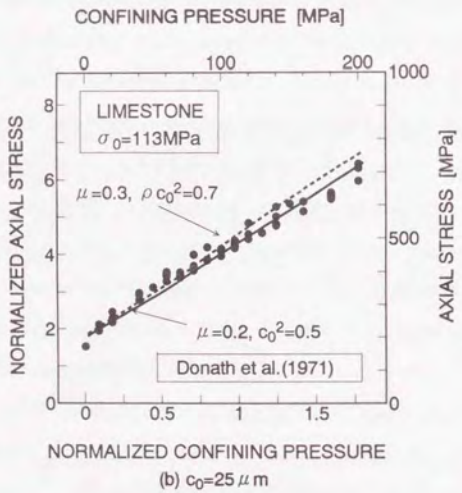

Figure 3.21 Comparison between experimental and theoretical failure envelopes for limestone. (a) $c_0 = 7\mu$m; (b) $c_0 = 25\mu$m.

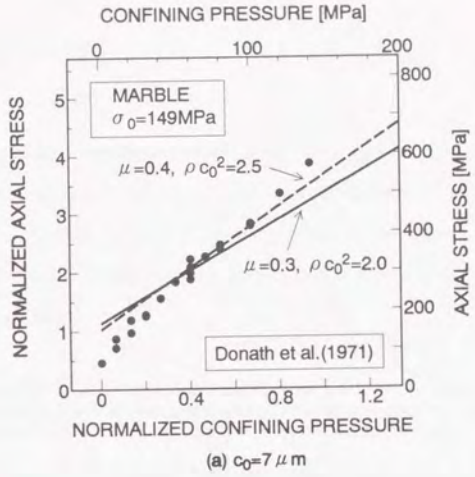

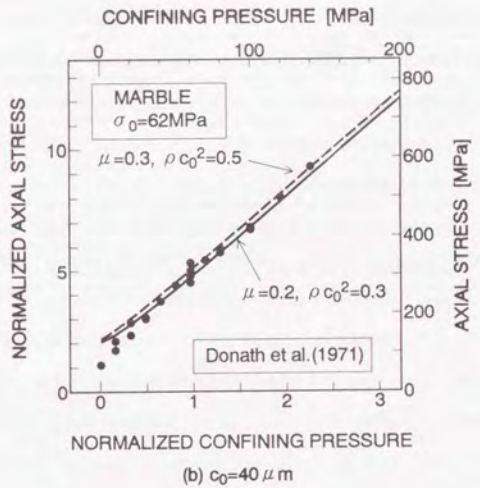

Figure 3.22 Comparison between experimental and numerical failure envelopes for Beldens marble. (a) $c_0 = 7\mu$m; (b) $c_0 = 40\mu$m.

Table 3.5 Model parameters used in numerical calculation for Beldens marble

Parameter	Value
Young's modulus	$E = 5.5 \times 10^4$ MPa
Poisson's ratio	$\nu = 0.25$
Fracture toughness	$K_c = 0.7$ MPam$^{1/2}$
Initial defect length	$c_0 = 7,\ 40\ \mu$m
Angle between initial defect and loading axis	$\theta = 45$ deg
Normalized crack density	$\rho c_0^2 = 0.3,\ 0.5,\ 2.0,\ 2.5$
Coefficient of friction	$\mu = 0.2,\ 0.3,\ 0.4$

3.7 Summary

In this chapter, a micromechanics-based continuum theory, named Interaction Field Theory (IFT), is formulated for the rate-independent behavior due to crack growth under compression. In addition, a micromechanics-based Continuum Damage Mechanics (CDM) is also formulated for the same problem to consider the difference between IFT from conventional CDM.

In IFT, the effects of interaction among microdefects in materials are evaluated directly in the evolution law of the microdefects (damage). To do this, the interaction tensor which characterizes the interaction effects is introduced and the integral equation for the interaction tensor is formulated.

From the comparison with CDM, it is shown that the constitutive relation of IFT depend on the stress and the damage parameter at whole points in the material. This means the constitutive relation of IFT is nonlocal. It is also shown that the nonlocality of the constitutive relation for the material with microstructure is due to the interaction effects of the microdefects.

While there are several attenuation functions of the conventional nonlocal models (see section 1.2.2), justification of the attenuation functions is mainly checked by phenomenological consideration based on the numerical simulations. Thus, it seems that the attenuation functions are introduced a- only techniques of numerical calculations and the justification is not clarified. In the present formulation, however, the attenuation function for the considered microdefect is derived rigorously with the method of micromechanics.

The numerical results presented here confirm that IFT can simulate localization phenomena as well as softening behavior, which is difficult to model by the conventional

CDM. In addition, the IFT is able to reproduce the transition from the shear failure mode to the axial splitting mode which is observed in laboratory test of actual brittle rocks as the confining pressure is decreased.

Prediction of the failure envelope of actual rocks under compression is attempted. For Westerly granite, the predicted results by IFT is plausible for confining pressure ranging from 20 to 600 MPa, where the shear failure mode occurs as the macroscopic failure mode. When the confining pressure is greater than 600 MPa, the failure envelope of experimental results deviates from the solution of IFT. This result suggests that for this range of the confining pressure the plastic deformation governs the macroscopic failure instead of the microcracking.

The strengths of other kinds of rocks under compression were also evaluated. Since all model parameters necessary for calculations were not available, the parameters, such as the density of microdefects and the coefficient of friction, were determined so as to fit the numerical results to the experimental data. Although the comparison should not necessarily be regarded as a direct support of the ability of the present theory because of involving free parameters, it seems that the values of the determined parameters are within the reasonable range.

References

M. F. Ashyby, S. D. Hallam and née Cooksley [1986], The failure of brittle solids containing small cracks under compressive stress states. *Acta Metall.*, 34(3):495–510.

B. K. Atkinson and D. G. Meredith [1987], Experimental fracture mechanics data for rocks and minerals, In B. K. Atkinson, editor, *Fracture Mechanics of Rocks*, chapter 11, pages 477–525. Academic Press, London.

N. Barton [1976], The shear strength of rock and rock joints. *Int. J. Rock Mech. Min. Sci. Geomech. Abstr.* , 13:255–279.

W. F. Brace [1965], Some new measurements of linear Compressibility of rocks. *J. Geophys. Res.*, 70(2):391–398.

W. F. Brace, Jr. B. W. Paulding, and C. Scholz [1966], Dilatancy in the fracture of crystalline rocks. *J. Geophys. Res.*, 71(16):3939–3953.

F. A. Donath, R. T. Faill and D. G. Tobin [1971], Deformation mode Fields in experimentally deformed rock. *Geol. Soc. Amer. Bull.*, 82:1441–1462.

J. M. Edmond and M. S. Paterson [1971], Volume changes during the deformation of rocks at high pressures. *Int. J. Rock Mech. Min. Sci.*, 9:161–182.

A. C. Eringen and D. G. B. Edelen [1972], On nonlocal elasticity. *Int. J. Engng. Sci.*, 10:233–248.

H. Fujii and M. Yamaguti [1980], Structure of singularities and its numerical realization in nonlinear elasticity. *J. Math. Kyoto Univ. (JMKYAZ)*, 20(3):489–590.

R. E. Goodman [1980], *Introduction to rock mechanics*, John Wiley & Sons, New York.

T. N. Gowd and F. Rummel [1980], Effect of confining pressure on the fracture behaviour of a porous rock. *Int. J. Rock Mech. Min. Sci. Geomech. Abstr.*, 17:225–229.

K. Hadley [1975], Comparison of calculated and observed crack densities and seismic velocities in Westerly granite. *Journal of Geophysical Research*, 81(20):3484–3494, 1975.

H. Horii and S. Nemat-Nasser [1983], Overall moduli of solids with microcracks: load-induced anisotropy. *J. Mech. Phys. Solids*, 31(2):155–177, 1983.

H. Horii and S. Nemat-Nasser [1985], Compression-induced microcrack growth in brittle solid: axial splitting and shear failure. *J. Geophys. Res.*, 90(B4):3105–3125, 1985.

H. Horii and S. Nemat-Nasser [1986], Brittle failure in compression: splitting, faulting and brittle-ductile transition. *Phil. Trans. R. Soc. Lond.*, A(319):337–374, 1986.

D. K. Hallbauer, H. Wagner, and N. G. W. Cook [1973], Some observations concerning the microscopic and mechanical behaviour of quartzite specimens in stiff, triaxial compression tests. *Int. J. Rock Mech. Min. Sci. Geomech. Abstr.*, 10:713–726.

H. B. Keller [1977], Numerical solution of bifurcation and nonlinear eigenvalue problems. In P. H. Rabinowitz, editor, *Applications of Bifurcation Theory*, pages 359–384, Academic Press, New York.

S. H. Kirby and A. K. Kronenberg [1984], Deformation of clinopyroxenite: evidence for a transition in flow mechanisms and semibrittle behavior. *J. Geophys. Res.*, 89(B5):3177–3192.

R. L. Kranz [1979], Crack growth and development during creep of Barre granite. *Int. J. Rock Mech. Min. Sci. Geomech. Abstr.*, 16:23–35.

K. Mogi [1966], Some precise measurements of fracture strength of rocks under uniform compressive stress. *Rock Mechanics and Engineering Geology*, 4:41–55.

W. C. Moss and Y. M. Gupta [1982], A constitutive model describing dilatancy and cracking in brittle rocks. *J. Geophys. Res.*, 87(B4):2985–2998.

N. I. Muskhelishvili [1953], *Some Basic Problems of the Mathematical Theory of Elasticity*. Noordhoff, Groningen, Translated from the Russian.

S. Nemat-Nasser and M. Obata [1988], A microcrack model of dilatancy in brittle materials. *J. Appl. Mech. ASME*, 55:24–35.

F. Ouchterlony et al. [1988], Suggested methods for determining the fracture toughness of rocks *Int. J. Rock Mech. Min. Sci. & Geomech. Abstr.*, 25(2):71–96.

R. N. Schock and H. C. Heard [1974], Static mechanical properties and shock loading response of Granite. *J. Geophys. Res.*, 79(11):1662–1666.

M. Shimada, A. Cho and H. Yukutake [1983], Fracture strength of dry silicate rocks at high confining pressures and activity of acoustic emission *Techtonophysics*, 96:159–172.

E. S. Sprunt and W. F. Brace [1974], Direct observation of microcavities in crystalline rocks. *Int. J. Rock Mech. Min. Sci. Geomech. Abstr.*, 11:139–150.

P. Tapponnier and W. F. Brace [1976], Development of stress-induced microcracks in Westerly granite. *Int. J. Rock Mech. Min. Sci. Geomech. Abstr.*, 103–112.

W. R. Wawersik and W. F. Brace [1971], Post-failure behavior of granite and diabase. *Rock Mechanics*, 61–85.

W. R. Wawersik and C. Fairhurst [1969], A study of brittle rock fracture in laboratory compression experiments. *Int. J. Rock Mech. Min. Sci.*, 7:561–575.

U. Yamaguti and Y. Nishimatu [1980], *Introduction to Rock Mechanics*, Tokyo Univ. Press, in Japanese.

M. D. Zoback and J. D. Byerlee [1975], The effect of cyclic Differential stress on dilatancy in Westerly granite under uniaxial and triaxial conditions *J. Geophys. Res.*, 80(11):61–85.

Chapter 4

Formulation for Behavior due to Time-Dependent Crack Growth

4.1 Introduction

Understanding of time-dependent behavior of rocks under various temperature and environmental conditions is of importance in the contexts of both geophysics and geotechnical engineering. Since most of tectonic stress generally does not vary rapidly, it is indispensable to understand the quasi-static behavior of rocks under constant stress states in order to consider behavior of the earth's crust. On the other hand, the engineering significance of the time-dependent behavior of rocks is found in the design for long-term stability of geothermal reservoirs, waste disposal facilities, compress gas stage and other geotechnical structures.

It is well known that the time-dependent behavior of brittle materials under low and constant stress states results from slow and stable growth of many microcracks.

The similar behavior due to the slow crack growth is found in glasses and ceramics, where the crack velocity is between about 10^{-10} and 10^{-2} m/s [Freiman, 1984]. This slow and stable crack growth can occur in many brittle materials even if the stress intensity factor at the crack tip is below its critical value—the fracture toughness of the materials. This phenomenon is called subcritical crack growth. (Note that the term "subcritical crack growth" represents extension of a single or isolated crack observed in crack growth rate testing such as the double torsion test, and does not mean evolution of many microcracks observed in creep tests.) Atkinson [1984] presented an extensive review of the experimental data on the subcritical crack growth in geological materials. He reported that the main parameters describing the subcritical crack growth are the fracture toughness K_c, the stress intensity factor K_I and the threshold stress intensity factor K_{th}. For various kinds of rocks, he illustrated the crack velocities as a function of the stress intensity factor K_I between K_{th} and K_c (K–v relation). The K–v relations depend on the chemical environments, such as temperature, moisture and pH [see, also Swanson, 1984]; and hence several mechanisms of the subcritical crack growth have been suggested such as stress corrosion, ion-exchange, dissolution and microplasticity. The most often cited mechanism for this time- and environment-dependent behavior is stress corrosion cracking, which is due to the join action of the high stress concentration at the tip of crack and a corrosive environment.

Kranz and coworker [1977, 1979, 1980] investigated experimentally the time-dependent behavior of Barre granite under constant uniaxial and triaxial stress states (ie. creep test). He reported effects of stress difference and confining pressure on the time to failure. The time to failure increases with decreasing stress difference at every confining pressure. In addition, employing scanning electron microscope he reported quantities related to microcracks, such as density, length and orientation at intervals of certain time during creep test. Although the orientations of crack-like flaws in unstressed samples are homogeneously distributed, the orientations of microcracks in

stressed samples are almost parallel to the direction of the maximum compression. This suggests that the same tension-crack model of microdefects as shown in Fig. 3.1 governs the failure process of rocks under constant stress states.

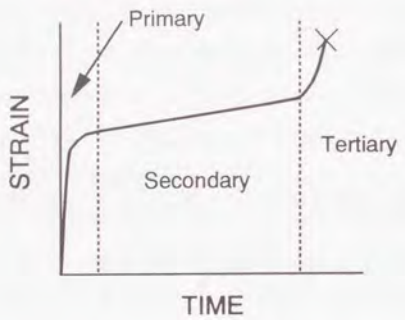

Figure 4.1 Schematic of strain as a function of time in a creep test of Barre granite [after Kranz, 1979].

Figure 4.1 shows a typical form of the relation between radial strain on the surface of a cylindrical sample of Barre granite and time during a creep test. This type of curve, in which strain or quantities related to deformation of samples is expressed as a function of time, is called a creep curve. The creep curve can be generally divided into three stages: (1) primary or transient creep, (2) secondary or steady creep and (3) tertiary creep. The tertiary creep is the onset of macroscopic fracture. Once samples of brittle rocks attain this tertiary stage, the samples fail unstably unless they are unloaded. Excepting the uniaxial tests, the final failure plane in the creep tests is inclined at an angle of about 20–30 deg, which is nearly equal to the angle of the final failure plane observed in the short-term fracture tests under constant strain rate. Thus, even for the case of the time-dependent behavior under constant stress states, the eventual macroscopic failure seems to result from the localization of microcracking, as is the case with short-term triaxial tests under constant strain or stress rate.

In this chapter, IFT is applied to creep of brittle materials under compressive stress states. The micromechanical model employed to formulate continuum theory for creep deformation of brittle materials is the same as the model of microdefects shown in the previous chapter for time-independent problem. Accordingly, the governing equations for the creep deformation of brittle materials are the same equations as given in the previous chapter except for the evolution law of microdefects. In the next section, thus, only the evolution law of time-dependent crack growth is introduced and the explanation of the other governing equations is omitted.

4.2 Evolution law

Many attempts have been made to describe K–v relation of the subcritical crack growth, and almost all the equations proposed are usually semi- or wholly-empirical [Atkinson, 1984]. The most widespread equation used to describe the subcritical crack growth in geological materials is the well-known power law:

$$\frac{dl}{dt} = A(K_I)^n, \quad \cdots\cdots (4.1)$$

where dl/dt is the crack velocity; A and n are experimentally determined constants, which depend on temperature and chemical environment, such as pH and moisture.

If the units of the crack velocity and the stress intensity factor in equation (4.1) are m/s and MPam$^{1/2}$, respectively, then the reported values of exponent n called the subcritical crack growth index lie between 30 to 46 for Westerly granite in liquid water at room temperature [Atkinson, 1984]. On the other hand, coefficient A in equation (4.1) is of the order 10^{-3}–10^{-12} based on the same experimental data. As another important parameter describing the subcritical crack growth, there is the threshold of the

stress intensity factor. However, the effect of the threshold on the subcritical crack growth is neglected in the following numerical calculations. There are two reason for this. First, for Westerly granite, no reported value of such limit is found in literatures and the reported crack velocities are as slow as 10^{-12} m/s. Secondly, the testing time required to establish the threshold may be extremely long, and thus the reported value of the threshold should not be regarded as a objective material parameter, even if the reported threshold is found.

4.3 Time-integration scheme

The procedure of discretization by finite element method is the same as one shown in the previous chapter, and thus only time-integration scheme is explained briefly in this section. After the short-term behavior of the material is computed by the numerical analysis method presented in the previous chapter, Euler's method is employed in order to allow the solution to be advanced from a time $t^{(s)}$ to time $t^{(s+1)} = t^{(s)} + \Delta t^{(s)}$, where superscripts (s) and $(s+1)$ denote successive times and $\Delta t^{(s)}$ is the time interval. In this method, the mean rate of change of time-dependent variables over the time interval is taken as the value at the beginning of the interval. Thus, from the evolution law [equation (4.1)], the increment of the damage parameter $\Delta l^{(s)}$ (the length of microdefects) occurring during time step $\Delta t^{(s)}$ is obtained as

$$\Delta l^{(s)} = A(K_I)^n \Delta t^{(s)}, \quad \cdots\cdots (4.2)$$

where the mode I stress intensity factor K_I is evaluated from equation (3.35) using the stress $\hat{\sigma}^{(s)}$, the pseudotraction $\sigma^{P(s)}$ and the damage parameter $l^{(s)}$ at time $t^{(s)}$. The total damage parameter $l^{(s+1)}$ at time $t^{(s+1)}$ is calculated by adding the incremental value to the previous total value:

$$l^{(s+1)} = l^{(s)} + \Delta l^{(s)}. \quad \cdots\cdots (4.3)$$

After all damage parameters in each finite element are calculated, stress $\hat{\sigma}^{(s+1)}$, strain $\hat{\epsilon}^{(s+1)}$ and displacement $\hat{u}^{(s+1)}$ at time $t^{(s+1)}$ are obtained by solving stiffness equation induced from conventional finite element procedure. Then, the pseudotraction $\sigma^{P(s+1)}$ at time $t^{(s+1)}$ is evaluated by solving the discretized consistency equation, which in matrix form is written as

$$(\boldsymbol{I} - \boldsymbol{\Gamma})\sigma^{P(s+1)} = \boldsymbol{\Gamma}\hat{\sigma}^{(s+1)}, \quad \cdots\cdots (4.4)$$

where $\boldsymbol{I}$ denotes the $3M \times 3M$ identity matrix, M is the total number of the finite elements and $\boldsymbol{\Gamma}$ is the $3M \times 3M$ matrix defined by

$$\boldsymbol{\Gamma} = \sum_{i,j}^{M,M} \int_{V_j} \rho\gamma(\bar{\boldsymbol{x}}^i|\boldsymbol{\xi})d\boldsymbol{\xi}, \quad \cdots\cdots (4.5)$$

in which V_j and $\bar{\boldsymbol{x}}^i$ denote the area of element–j and the centroid of element–i, respectively.

At this stage all time-dependent variables have been updated to time $t^{(S+1)}$. The above time-marching scheme is repeated for each time step until solution is obtained for the desired time duration.

4.4 Numerical Results and Discussion

The numerical computations are carried out to reproduce the creep tests of Barre granite by Kranz [1980]. The model parameters used in the following calculations are

Table 4.1 Model parameters used in numerical calculation for creep test of Barre granite

Parameter	Value
Young's modulus	$E = 6.0 \times 10^4$ MPa
Poisson's ratio	$\nu = 0.3$
Fracture toughness	$K_c = 1.0$ MPam$^{1/2}$
Initial defect length	$c_0 = 27$ μm
Normalized crack density	$\rho c_0^2 = 0.15$
Initial defect angle	$\theta = 45$ deg
Coefficient of friction	$\mu = 0.2$
Subcritical crack index	$n = 30$
Coefficient A in eq.(4.1)	$A = 10^{-7}$, 10^{-6}, 10^{-5}

listed in Table 4.1, where Young's modulus, Poisson's ratio and the average length of the initial defects of Barre granite are reported by Kranz and Scholz [1977] and Kranz [1979]. The reported values of the fracture toughness of Barre granite range from 0.74 to 1.5 MPam$^{1/2}$ [Atkinson, 1984]. On the other hand, those of the subcritical crack index "n" in equation (4.1) for Barre granite are not available, but for Westerly granite the reported values ranges from 35.9 to 69, which are obtained by using double torsion specimens at room temperature in 30–50 % relative humidity [Atkinson, 1984; Swanson, 1984].

However the other model parameters of Barre granite, such as the crack density and the frictional coefficient, are not reported. Thus, the crack density and the frictional coefficient of Barre granite is determined by fitting the short-term strength obtained by numerical calculations to the experimental strengths. Figure 4.2 shows the comparison between numerical and experimental strengths of Barre granite, in which the

experimental strengths of Barre granite are reported by Kranz [1980] and the numerical strengths are calculated by IFT for the frictional coefficient 0.2 and the crack density 0.15.

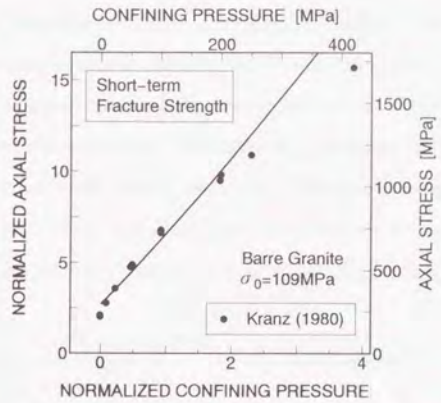

Figure 4.2 Comparison between the numerical and experimental strengths of short-term fracture test for $\mu = 0.2$, $\rho c_0^2 = 0.15$.

The used mesh configuration is the same model as shown in Fig. 3.14(a) except for a boundary condition of the top boundary in the specimen. For the present case, the traction at the top boundary is assigned to a specific value instead of prescribing the displacement so as to keep the axial stress constant during a creep test.

Figure 4.3 shows the relation between normalized crack length (damage parameter) and time for the confining pressure $p_c = 100$ MPa. In this calculation, the applied axial stress $\hat{\sigma}_1$ during the creep test is held constant so that the normalized stress difference $(\hat{\sigma}_1 - p_c)/(\hat{\sigma}_1 - p_c)_{max}$ is equal to 0.91, where $(\hat{\sigma}_1 - p_c)_{max}$ is the maximum stress difference obtained by the short-term fracture test with constant strain rate at the corresponding confining pressure. In the primary creep, all damage parameters in the elements evolve rapidly, because the stress intensity factors in all elements are nearly equal to the fracture toughness, which makes the crack velocities calculated from

equation (4.1) maximize. For the present micromechanical model shown in Fig. 3.1(a), the stress intensity factor decrease with increasing the crack length under constant stress states, which mechanism bring about transition from the primary creep into the secondary creep. Even for the secondary creep, the distribution of damage parameters is not homogeneous in the specimen. From the onset of the tertiary creep, the evolution of damage parameters is accelerated in several elements, and eventually the damage parameters in the elements evolve unstably. This localization of damage evolution and the associated instability are considered to have resulted from the effects of interaction among microdefects. In the following numerical calculations, the occurrence of the unstable evolution of damage parameters is interpreted as the onset of the macroscopic failure.

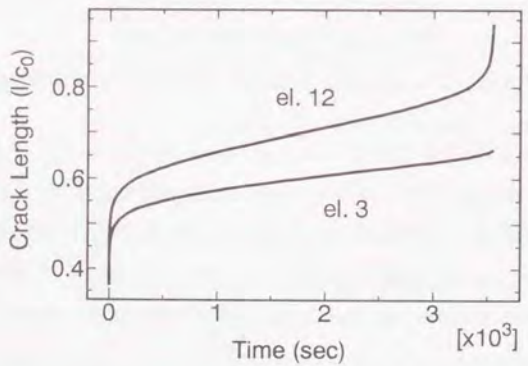

Figure 4.3 Evolution of normalized crack length (damage parameter) as a function of time for $A = 10^{-5}$, normalized stress difference $(\dot{\sigma}_1 - p_c)/(\dot{\sigma}_1 - p_c)_{max} = 0.91$ and confining pressure $p_c = 100$ MPa.

If the effects of interaction among microdefects are neglected on the determination of crack extension, it is quite obvious that no unstable crack growth occurs and that the distribution of the damage parameters is uniform because of homogeneous stress states. Thus, in conventional creep analyses based on phenomenological consideration,

the conditions that specifies macroscopic failure are introduced by, for example, a critical creep strain [Wilshire, 1991]. However, since the inelastic strain during creep is essentially due to the crack opening or void nucleation, the critical strain itself depends on applied stress. Once stress states varies (eg. under different confining pressures), the critical strain which defines failure condition varies accordingly. Consequently, for each corresponding stress state, different failure conditions must be determined. However, in the present theory, no phenomenological failure condition is introduced and macroscopic failure is reproduced as the unstable evolution of damage parameters.

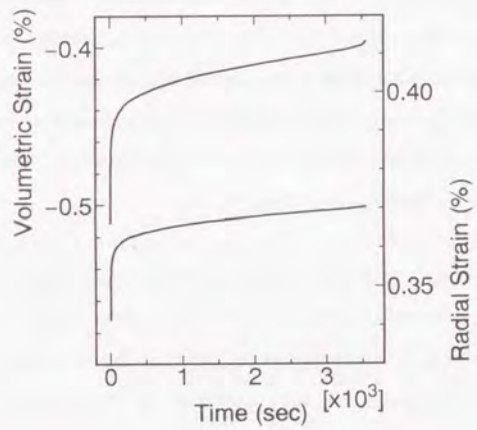

Figure 4.4 Creep curves of volumetric strain $\dot{\epsilon}_1 + 2\dot{\epsilon}_2$ and radial strain $\dot{\epsilon}_2$ for $n = 30$ for $A = 10^{-6}$, normalized stress difference $(\dot{\sigma}_1 - p_c)/(\dot{\sigma}_1 - p_c)_{max} = 0.91$ and confining pressure $p_c = 100$ MPa.

Figure 4.4 shows the creep curves of both overall volumetric strain $\dot{\epsilon}_1 + 2\dot{\epsilon}_2$ and radial strain $\dot{\epsilon}_2$ under the same loading condition as shown in Fig. 4.3. The majority of the creep strain occurs just after the initial loading and immediately before the macroscopic failure, which tendency agrees with creep curves observed in experimental

observation. According to experimental results by Kranz [1980], the volumetric and radial strain at the onset of the tertiary creep under the same loading conditions are 0.90 and 1.18 %, respectively. The experimental strains are obtained from electrical resistance strain gages cemented to the cylindrical samples, while the numerical results are calculated from the two dimensional model under plane strain condition. Thus, the direct comparison of the calculated strains with the experimental ones is not possible. However, calculated dilation at the onset of the tertiary creep is seemed to be somewhat smaller than the experimental results.

Figure 4.5 shows the logarithm of creep rupture time t_f in seconds as a function of the normalized stress difference $(\hat{\sigma}_1 - p_c)/(\hat{\sigma}_1 - p_c)_{max}$ at the confining pressures (a) $p_c = 0$, (b) 53 and (c) 100 MPa. In these figures, the experimental data for Barre granite reported by Kranz [1980] are also plotted as the closed circles. The numerical calculations are carried out for $A = 10^{-5}$, 10^{-6} and 10^{-7}, which is the coefficient in the evolution law [equation (4.1)].

The experimental data for uniaxial creep tests show considerably more scatter than those for tests under confining pressure. The fluctuations in failure time under uniaxial compression may be attributed to the fact that the creep failure under uniaxial compression occurs owing to the same mechanism as short-term fracture under uniaxial compression. In the short-term fracture tests under uniaxial compression, the axial splitting occurs as the macroscopic failure mode. As discussed in the previous chapter, the mechanism of the axial splitting is considered to be unstable extension of a single or a few tension cracks. Thus, as with the axial splitting in the short-term fracture tests under uniaxial compression, it is considered that the creep failure under uniaxial compression largely depend on both length and orientation of the initial defect which is most likely to nucleate tension cracks in each sample. Since the distribution of the length and orientation of initial defects is different in sample to sample, the times

to failure of uniaxial creep tests are more scatter than those of tests under confining pressure.

The times to failure decrease with increasing the normalized stress difference, which tendency agrees with the experimental results. In particular, for the cases of the creep tests applying confining pressure as shown in Fig. 4.5(a) and (b), the slopes of the theoretical curves are fair agreement with those of the experimental data. However, the values of "A" in equation (4.1) obtained by fitting the numerical results to the experimental data depend on the confining pressures, and are 10^{-6} and 10^{-5} for the confining pressure 53 and 100 MPa, respectively. This may suggests that the confining pressure affects the subcritical crack growth due to stress corrosion. In the proposed theory, the effect of the confining pressure on the crack velocity is considered by calculating the stress intensity factor as a function of the confining pressure, which reflects the frictional sliding of the initial defect. However, the evolution law [equation (4.1)] is derived by the experiments of which samples are not applied confining pressure. In order to clarify the effect of the confining pressure on the stress corrosion, experiments designed to investigate the effect of the confining pressure on the stress corrosion are needed.

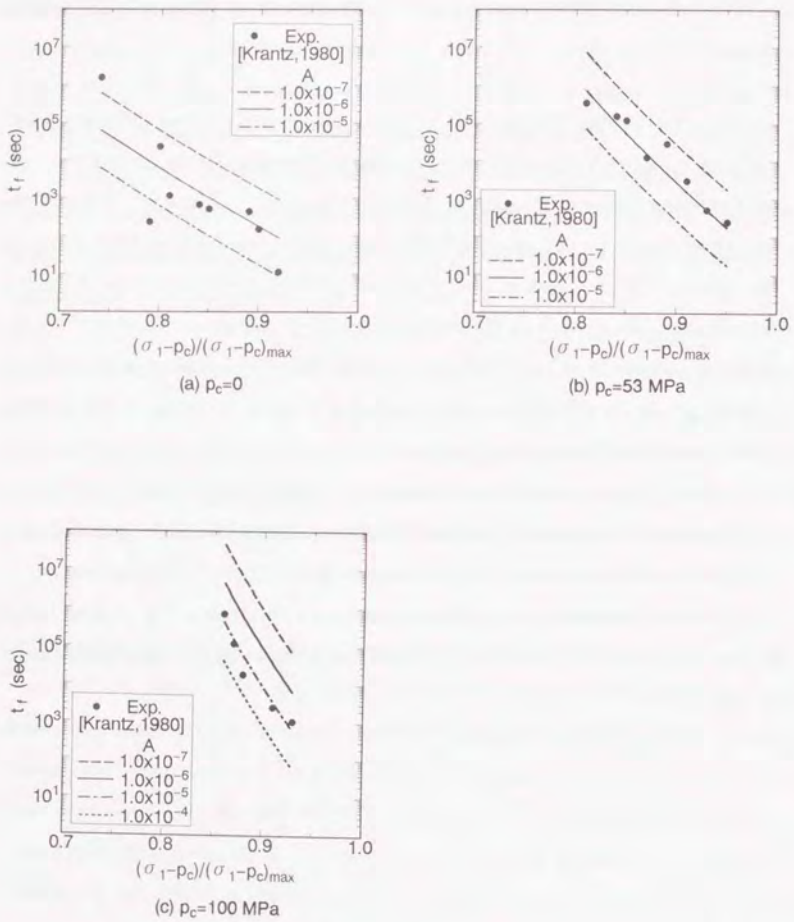

Figure 4.5 Failure time vs normalized stress deference at confining pressures (a)$p_c = 0$, (b)53 and (c)100 MPa for Barre granite.

4.5 Summary

In this chapter, IFT is applied for the time-dependent behavior of brittle material under compressive stress states. Numerical examples are given, which is intended to reproduce creep tests of Barre granite under constant stress states.

Numerical results confirm that the proposed continuum theory reproduce typical shapes of creep curves observed in laboratory tests; namely, the primary, secondary and tertiary stages of creep deformation. In the primary creep, all damage parameters in a specimen evolve rapidly, because the stress intensity factors in the elements nearly equal to the fracture toughness. The transition from the primary into the secondary creep stages results from the mechanism that the stress intensity factor decreases with increasing the crack length under constant stress states. The main mechanism of steep increase in strains and damage during the tertiary creep is due to the effects of the interaction among microdefects. In the numerical calculations, the eventual macroscopic failure following the tertiary creep is reproduced by the unstable evolution of the damage parameters.

Comparisons are made between predicted and experimental rupture-times. The failure time decreases with increasing the normalized stress difference, which tendency agrees with experimental results.

References

B. K. Atkinson [1984], Subcritical crack growth in geological materials. *J. Geophys. Res.* , 89(B6):4077–4114.

S. W. Freiman [1984], Effects of chemical environments on slow crack growth in glasses and ceramics. *J. Geophys. Res.* , 89(B6):4072–4076.

R. L. Kranz and C. H. Scholz [1977], Critical dilatant volume of rocks at the onset of tertiary creep. *J. Geophys. Res.* , 82(30):4893–4898.

R. L. Kranz [1979], Crack growth and development during creep of Barre Granite. *Int. J. Rock Mech. Min. Sci. & Geomech. Abstr.*, 16:23–35.

R. L. Kranz [1980], The effect of confining pressure and stress difference on static fatigue of granite. *J. Geophys. Res.*, 85(B4):1854–1866.

P. L. Swanson [1984], Subcritical crack growth and other time- and environment-dependent behavior in crustal rocks. *J. Geophys. Res.* , 89(B6):4137–4152.

B. Wilshire [1991], Microscopic models and macroscopic constitutive laws for high temperature creep and creep fracture of metallic and ceramic materials. In A.C.F. Cocks and A.R.S. Ponter, editors, *Mechanics of Creep Brittle Materials.* , 2:112–123, Elsevier.

Chapter 5

Formulation for Behavior of Granular Materials

5.1 Introduction

The main deformation mechanisms of granular materials are slips and associated relocation of particles. As a well-known deformation characteristic of granular materials, the relocation of particles induces dilation even if the hydrostatic stress is constant. In addition, with the increase in external loads, the deformation of the granular materials loses homogeneity, and the localization of deformation into thin layers occurs. These layers are called shear bands or zones, because large shearing deformation is produced in the layers.

Since the shear band formation extensively affects the load-carrying capacity of granular materials, many element tests under various boundary conditions and stress paths have been undertaken in order to induce, for instance, the conditions of forma-

tion of the shear bands and objective constitutive relations of the granular materials [e.g., Mandl, 1976; Tatuoka et al., 1986, 1988; Negussey and Vaid, 1990; Drescher, 1990; Wu and Kolymbas, 1991]. When these conditions and constitutive relations are derived from experimental observations, the strain and stress fields before the shear band formation are assumed to be homogeneous inside the specimen. However microscopic observations of sand specimens reveal that the distribution of deformation loses homogeneity at early stages of loading before the shear band formation. Thus, the assumption of homogeneity before the shear band formation does not hold. On the other hand, in order to simulate behavior of sand samples up to post-peak regime by solving boundary value problems using phenomenological constitutive relation, it is necessary to obtain the constitutive relation within the shear bands besides overall constitutive relations of specimens with the shear bands.

Recently, qualitative information about deformation within sand specimens containing the shear bands is reported with new observation methods, such as X-ray photographs, laser speckle method, stereophotogrammetric method [Butterfield, 1970] and image analysis, etc. On the basis of the observation with X-ray photographs, Vardoulakis and Graf [1985] reported that the thickness of shear bands in sand is about 13–20 times the mean grain diameter. Tatuoka and co-workers [1990] employed the laser speckle method, and reported qualitative information on surface displacements of sand specimens. More recently, Yoshida [1992] reported the following process of the shear band formation based on the observation of plane strain condition tests with image analysis. The strain localization occurs in the center of specimens before the peak stress ratio. In the pre-peak regime the distribution of strain is not homogeneous in the specimen, and the shear strain is localized in the several strips intersecting each other. At almost peak stress ratio, one of these strips evolves and the others stop their evolution. But the position of the active strip does not coincide with the that of the final shear band. In addition to these observations, Yoshida reported the following

constitutive relations of the shear bands: (a) the relations between the stress averaged over the whole specimen and the tangential displacement gap across the shear bands and (b) the relations between the tangential and the normal displacement gap.

As an another approach, numerical simulation of plane assemblies of disks offers complete quantitative information on microscopic features of particles, such as contact density, contact orientations and magnitudes of contact forces [Cundall, 1989; Rothenburg and Bathurst, 1989; Bardet and Proubet, 1991]. These studies are intended to clarify the relations between these microscopic quantities and macroscopic quantities such as stress tensor or strain, and deduce the macroscopic constitutive relation of granular materials from microscopic events.

Although considerable studies are being devoted toward formulating boundary value problems using phenomenological constitutive relations based on experimental observations, the present study uses a constitutive relation based on micromechanics. In this chapter, the application of IFT to granular materials such as sand is introduced. The procedure formulating the governing equations for granular materials is almost same as that for the behavior of brittle materials presented in the previous chapter. In the first place, a micromechanical model which represent the mechanical behavior of granular materials is introduced. After that, the governing equations of the proposed theory is derived from homogenization of an elastic medium containing this micromechanical model. Several numerical results are presented, and finally the applicability of IFT for granular materials is discussed.

5.2 Microslip Model

To study mechanism of strain localization in granular materials, a micromechanical model, called microslip model, has been proposed by Shi and Horii [1989]. In the present study, to formulate continuum theory for the behavior of granular materials, the microslip model is adopted as a micromechanical model and is introduced briefly in this subsection. The microslip consists of a initial defect and two slip zones. The initial defect of length $2a$ is a crack-like slit, on which frictional sliding occurs due to far-field principal stresses σ_1^∞ and σ_2^∞. This frictional sliding nucleates the two slip zones of length l from the tips of the initial defect; see Fig. 5.1.

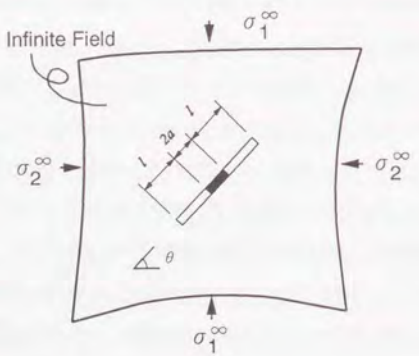

Figure 5.1 Microslip model

The conditions of the frictional sliding are assumed to be the following expressions,

$$\begin{aligned} \sigma_{xy} &= (\sigma_{yy} + \sigma_d)\tan\phi_0, \quad \text{(on initial defect)}, \\ \sigma_{xy} &= (\sigma_{yy} + \sigma_d)\tan\phi_c, \quad \text{(on slip zone)}, \end{aligned} \qquad \cdots\cdots (5.1)$$

where σ_{xy} is the shear stress and σ_{yy} is the normal stress on the surfaces of the microslip; ϕ_0 and ϕ_c ($\phi_c > \phi_0$) are the frictional angles on the initial defect and the slip zones,

respectively; σ_d is called a dilatancy stress. The dilatancy stress, which acts to open the surfaces of the microslips, is introduced to represent the effect of local dilatancy due to asperity of particles during the sliding. Since the amount of the local dilatancy depend on that of sliding, Shi and Horii assume that the magnitude of the dilatancy stress is proportional to the half length of the microslip;

$$|\sigma_d| = \alpha_d c, \qquad \cdots\cdots (5.2)$$

where α_d is called the dilatancy coefficient.

However, it is not realistic for the dilation due to sliding to keep increasing linearly with the increase in the sliding. Hence, for the present formulation, hence, the dilatancy stress is given by an alternative expression:

$$\sigma_d = -\alpha_d \sigma_0 (c/a - 1)^m, \qquad \cdots\cdots (5.3)$$

where α_d and m are constants and σ_0 is a reference stress, which is assigned to the confining pressure in the following numerical calculation. The relations between normalized dilatancy stress $-\sigma_d/(\alpha_d\sigma_0)$ and normalized microslip length c/a are shown in Fig. 5.2.

The direction of the microslip is assumed to be $\theta = \pm(\pi/4 + \phi_c/2)$ with respect to the direction of the minimum compression σ_2^∞, because the frictional sliding is most likely to occur in this direction, in which the ratio $|\sigma_{xy}/\sigma_{yy}|$ takes its maximum value.

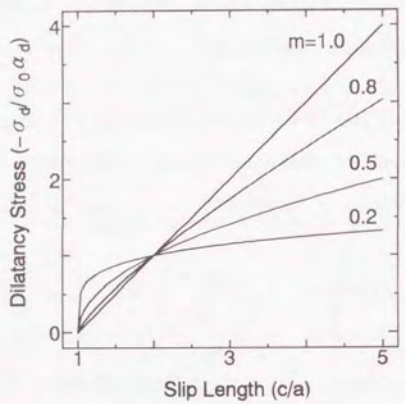

Figure 5.2 Relation between normalized dilatancy stress $-\sigma_d/(\sigma_0\alpha_d)$ and normalized slip length c/a

5.3 Homogenization and Governing Equations

Similarly to the formulation of IFT for behavior due to crack growth under compression, the microslips are supposed to be distributed over a elastic medium with a certain density. The microslips are classified into two systems in which the angles of the directions of the microslips are $\theta_I = (\pi/4+\phi_c/2)$ and $\theta_{II} = -(\pi/4+\phi_c/2)$ with respect to the direction of the minimum principal compression σ_2^∞; see Fig. 5.3. Each of the densities of the microslips in the systems is assumed to be a same value ρ, where the density ρ means the number of the microslips per unit area. The elastic medium containing many microslips is homogenized into a equivalent continuum based on the concept of averaging over local volume elements in the medium.

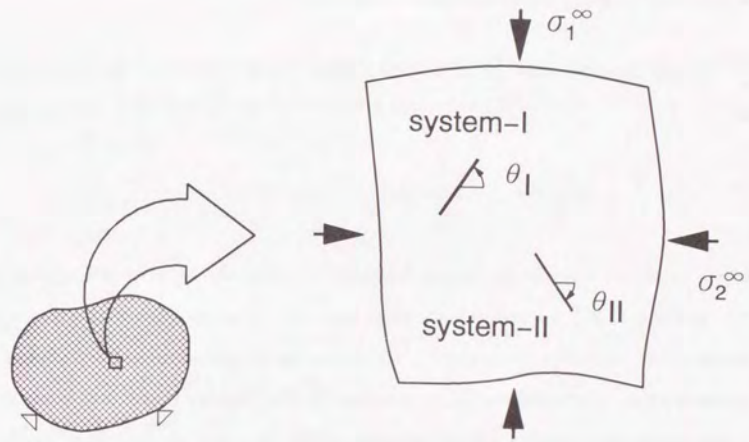

Figure 5.3 Two systems of microslips.

Because the equilibrium equation and the strain–displacement relation of the equivalent continuum are the same equations as shown in the previous chapter, the explana-

tion of the formulating these equations is omitted out in this chapter. The formulation of the other governing equations for the equivalent continuum is explained in the following order: beginning with the stress–strain relation of the considered model, going through the consistency equation and ending with the evolution law of the microslips.

5.3.1 Stress–strain relationship

Before formulating the stress–strain relation of the equivalent continuum, the basic assumptions are introduced. It is assumed that the relation between the average stress and strain over representative volume elements in the elastic medium containing the microslips offers the stress–strain relation of the equivalent continuum. In deriving the average stress–strain relation of the elastic medium containing the microslip, the effects of interaction among the microslips are neglected.

As mentioned in equation (3.25), the average strain due to the microslips is given by

$$\hat{\varepsilon}^* = \frac{1}{V_e}\int_S \frac{1}{2}([u]\otimes n + n\otimes[u])ds, \quad \cdots\cdots (5.4)$$

where $[u] = u^+ - u^-$ is the displacement gap between the surfaces of the microslip; see equation (3.25) for the definitions of the other symbols. Since the interaction effects of the microslips are neglected, the displacement gaps of many microslips in the representative volume element V_e are evaluated by the following procedure. Considering elastic mediums containing a single microslip under the action of the average stress, the displacement gap of the microslip in the elastic mediums is calculated. and superposed to the displacement gaps of the other microslips. Then, the total displacement gap is expressed in terms of the average stress and the dilatancy stress, and accordingly the average strain due to the microslips is expressed by the following form:

$$\hat{\varepsilon}^* = \boldsymbol{C}^* : \hat{\sigma} + \hat{\varepsilon}^{**}, \quad \cdots\cdots (5.5)$$

where $\hat{\sigma}$ is the average stress and $\hat{\varepsilon}^{**}$ is the average strain due to the dilatancy stress, which does not depend on the average stress explicitly.

The average elastic strain $(\hat{\varepsilon} - \hat{\varepsilon}^*)$ is related to the average stress by Hook's law;

$$\hat{\sigma} = \boldsymbol{D}^e : (\hat{\varepsilon} - \hat{\varepsilon}^*), \quad \cdots\cdots (5.6)$$

where $\boldsymbol{D}^e$ is the elastic moduli of the matrix, which is assumed to be locally isotropic. By substituting equation (5.5) into (5.6), we have

$$(\boldsymbol{I} + \boldsymbol{D}^e : \boldsymbol{C}^*) : \hat{\sigma} = \boldsymbol{D}^e : \hat{\varepsilon} - \boldsymbol{D}^e : \hat{\varepsilon}^{**}, \quad \cdots\cdots (5.7)$$

where $\boldsymbol{I}$ is the fourth order identity tensor. Equation (5.7) stands for a system of linear equations for unknowns $\hat{\sigma}$, and solving this system of the equations, the stress–strain relation is given by

$$\hat{\sigma} = \boldsymbol{D}^{ep} : \hat{\varepsilon} + \hat{\sigma}^*, \quad \cdots\cdots (5.8)$$

where

$$\boldsymbol{D}^{ep} = (\boldsymbol{I} + \boldsymbol{D}^e : \boldsymbol{C}^*)^{-1} : \boldsymbol{D}^e, \quad \cdots (5.9)$$

$$\hat{\sigma}^* = -\boldsymbol{D}^{ep} : \hat{\varepsilon}^{**}. \quad \cdots (5.10)$$

For the present two dimensional problem, the average stress and strain tensors are reduced into the following vector forms: $\hat{\sigma} = \{\hat{\sigma}_{11}, \hat{\sigma}_{22}, \hat{\sigma}_{12}\}^T$, $\hat{\epsilon} = \{\hat{\varepsilon}_{11}, \hat{\varepsilon}_{22}, 2\hat{\varepsilon}_{12}\}^T$, and accordingly the tensors $\boldsymbol{I}, \boldsymbol{D}^e, \boldsymbol{D}^{ep}$ and $\boldsymbol{C}^*$ are also reduced into 3×3 matrices.

The average strain $\hat{\boldsymbol{\epsilon}}^*$ due to the microslips for the global coordinate (x_1, x_2) consists of two elements $\hat{\boldsymbol{\epsilon}}^{*I}$, $\hat{\boldsymbol{\epsilon}}^{*II}$ caused by the microslips for system I and II, respectively. Transforming the average strain in the local coordinate systems into the global one and summing the average strain due to the microslips in both systems, $\hat{\boldsymbol{\epsilon}}^*$ is expressed by

$$\hat{\boldsymbol{\epsilon}}^* = \boldsymbol{R}^T(\theta_I)\hat{\boldsymbol{\epsilon}}^{*I} + \boldsymbol{R}^T(\theta_{II})\hat{\boldsymbol{\epsilon}}^{*II}, \qquad \cdots\cdots (5.11)$$

where $\hat{\boldsymbol{\epsilon}}^{*\alpha} = \{\hat{\varepsilon}^{*\alpha}_{xx}, \hat{\varepsilon}^{*\alpha}_{yy}, 2\hat{\varepsilon}^{*\alpha}_{xy}\}^T$, $(\alpha = I, II)$ and $\boldsymbol{R}$ is the transformation matrix defined by

$$[R_{ij}(\theta)] = \begin{bmatrix} \cos^2\theta & \sin^2\theta & 2\cos\theta\sin\theta \\ \sin^2\theta & \cos^2\theta & -2\cos\theta\sin\theta \\ -\cos\theta\sin\theta & \cos\theta\sin\theta & \sin^2\theta - \cos^2\theta \end{bmatrix} \qquad \cdots\cdots\cdots\cdots\cdots (5.12)$$

with $\theta_I = -\theta_{II} = \pi/4 - \phi_c/2$.

The average strain caused by the microslips in system α, $(\alpha = I, II)$ for the local coordinate is expressed by the same form as shown in equation (5.5);

$$\hat{\boldsymbol{\epsilon}}^{*\alpha} = \boldsymbol{C}^{**\alpha}\hat{\boldsymbol{\sigma}}^{\alpha} + \hat{\boldsymbol{\epsilon}}^{**\alpha}, \qquad (\alpha = I, II), \qquad [\alpha : \text{not summed}], \cdots\cdots\cdots (5.13)$$

where $\hat{\boldsymbol{\sigma}}^{\alpha} = \{\hat{\sigma}^{\alpha}_{xx}, \hat{\sigma}^{\alpha}_{yy}, \hat{\sigma}^{\alpha}_{xy}\}^T$ denotes the average stress for the local coordinate (x^α, y^α). For system I, the nonvanishing components of the matrix $\boldsymbol{C}^*$ and the vector $\hat{\boldsymbol{\epsilon}}^{**\alpha}$ are

$$\begin{aligned} C^{*I}_{32} &= -\frac{2\rho}{E'}\{\pi c_I^2 \tan\phi_c - 4ac_I(\tan\phi_c - \tan\phi_0)\}, \\ C^{*I}_{33} &= \frac{2\rho}{E'}\pi c_I^2, \\ \hat{\varepsilon}^{**I}_{yy} &= -\frac{2\rho}{E'}\pi c_I^2 \sigma_d^I \end{aligned}$$

and

$$\hat{\varepsilon}^{**I}_{xy} = -\frac{2\rho}{E'}\{\pi c_I^2 - 4ac_I(\tan\phi_c - \tan\phi_0)\}\sigma_d^I,$$

while for system II the components are

$$\begin{aligned} C^{*II}_{32} &= \frac{2\rho}{E'}\{\pi c_{II}^2 \tan\phi_c - 4ac_{II}(\tan\phi_c - \tan\phi_0)\}, \\ C^{*II}_{33} &= \frac{2\rho}{E'}\pi c_{II}^2, \\ \hat{\varepsilon}^{**II}_{yy} &= -\frac{2\rho}{E'}\pi c_{II}^2 \sigma_d^{II} \end{aligned}$$

and

$$\hat{\varepsilon}^{**II}_{xy} = \frac{2\rho}{E'}\{\pi c_{II}^2 - 4ac_{II}(\tan\phi_c - \tan\phi_0)\}\sigma_d^{II},$$

where c_α, $(\alpha = I, II)$ is half the length of the microslip in system α and σ_d^α is the dilatancy stress defined by equation (5.1) with c_α substituted for c.

Since the average stress for the local coordinate is expressed by

$$\hat{\boldsymbol{\sigma}}^{\alpha} = \boldsymbol{R}(\theta_\alpha)\hat{\boldsymbol{\sigma}}, \qquad \cdots\cdots (5.14)$$

substituting equation (5.13) into (5.11), the expressions of the matrix $\boldsymbol{C}^*$ and the vector $\boldsymbol{\epsilon}^{**}$ are obtained as

$$\boldsymbol{C}^* = \boldsymbol{R}^T(\theta_\alpha)\boldsymbol{C}^{**\alpha}\boldsymbol{R}(\theta_\alpha), \qquad \cdots\cdots (5.15)$$

$$\boldsymbol{\epsilon}^{**} = \boldsymbol{R}^T(\theta_\alpha)\boldsymbol{\epsilon}^{**\alpha}. \qquad \cdots\cdots (5.16)$$

Using equations (5.15) and (5.16), the stress–strain relation for the considered two dimensional problem can be rewritten as the following matrix-vector form similar to equation (5.5):

$$\hat{\boldsymbol{\sigma}} = \boldsymbol{D}^{ep}\hat{\boldsymbol{\epsilon}} + \hat{\boldsymbol{\sigma}}^*, \qquad \cdots\cdots (5.17)$$

where

$$\boldsymbol{D}^{ep} = (\boldsymbol{I} + \boldsymbol{D}^e\boldsymbol{C}^*)^{-1}\boldsymbol{D}^e, \qquad \cdots\cdots (5.18)$$

$$\hat{\boldsymbol{\sigma}}^* = -\boldsymbol{D}^{ep}\hat{\boldsymbol{\epsilon}}^{**}. \qquad \cdots\cdots (5.19)$$

5.3.2 Consistency equation

Before formulating the consistency equation for continuously distributed microslips, we follow the approach of Shi and Horii for discrete systems of the microslips, but do not limit the present formulation to the case of the parallel microslips. Figure 5.4 shows elastic medium containing two microslips, microslip α and microslip β, under farfield principal stresses σ_1^∞ and σ_2^∞. As mentioned in section 5.2, the boundary conditions [equation (5.1)] are satisfied along each of the microslips and the dilatancy stress defined by equation (5.3) is applied on the surfaces of the microslips as a normal component.

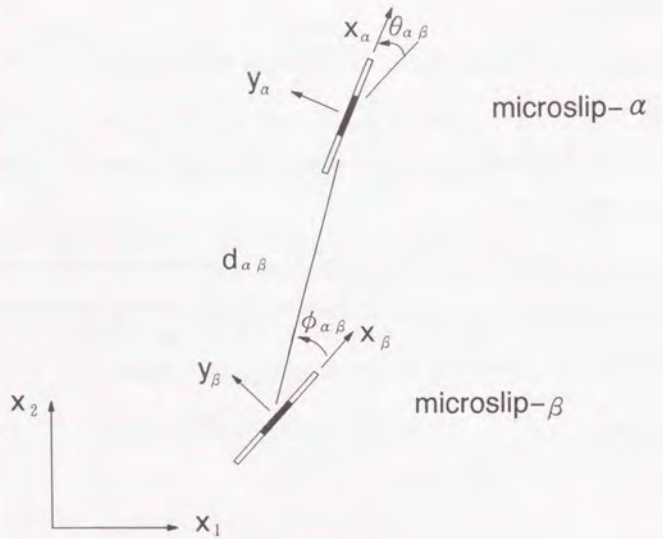

Figure 5.4 Discrete system of two microslips.

The original problem illustrated in Fig. 5.4 is decomposed into a homogeneous problem without the microslip and two subproblems with the single microslip; see Fig 5.5 (b),(c) and (d). To satisfy the boundary conditions of the original problem when superposing the homogeneous problem and the subproblems, the following tractions must be applied on the surfaces of the microslip in each subproblem i, $(i = \alpha, \beta)$, as a shear component

$$\begin{aligned} \tau &= -\sigma_{xy}^{\infty i} - \sigma_{xy}^{Pi} + (\sigma_{yy}^{\infty i} + \sigma_{yy}^{Pi} + \sigma_d^i)\tan\phi_0, \quad \text{(on initial defect)}, \\ \tau &= -\sigma_{xy}^{\infty i} - \sigma_{xy}^{Pi} + (\sigma_{yy}^{\infty i} + \sigma_{yy}^{Pi} + \sigma_d^i)\tan\phi_c, \quad \text{(on slip zone)}, \end{aligned} \qquad \cdots\cdots (5.20)$$

where $\sigma_{yy}^{\infty i}$, $\sigma_{xy}^{\infty i}$ and σ_{yy}^{Pi}, σ_{xy}^{Pi} are the stresses at the position of the microslip i in the homogeneous problem and the subproblem j, $(j \neq i)$, respectively. (Note that the microslip i exists actually neither in the homogeneous problem nor in the subproblem j.) The stresses σ_{yy}^{Pi} and σ_{xy}^{Pi}, called pseudotractions, are generated by the existence of the other microslip in the other subproblem.

Each of the subproblems can be further decomposed into two subsidiary problems illustrated in Fig. 5.6. In the subsidiary problem 1, the traction applied on the whole surface of the microslip is

$$\tau = -\sigma_{xy}^{\infty\beta} - \sigma_{xy}^{P\beta} + (\sigma_{yy}^{\infty\beta} + \sigma_{yy}^{P\beta} + \sigma_d^\beta)\tan\phi_c, \qquad (|x| \leq c),$$

while in the subsidiary problem 2, the following traction is applied only on the initial defect;

$$\tau = -(\sigma_{yy}^{\infty\beta} + \sigma_{yy}^{P\beta} + \sigma_d^\beta)(\tan\phi_c - \tan\phi_0), \qquad (|x| \leq a).$$

Assuming $a/c_\beta \ll 1$, the effects of the traction on the initial defect can be estimated as a concentrated force, and then the stress function of the subproblem β becomes

$$\Phi'_\beta(z_\beta) = -\frac{1}{2\pi i\sqrt{z_\beta^2 - c_\beta^2}} \int_{-c_\beta}^{c_\beta} \frac{\sqrt{t^2 - c_\beta^2}}{t - z_\beta}.$$

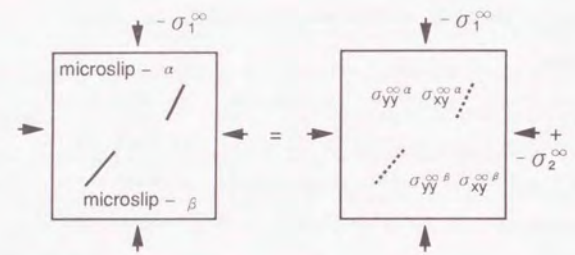

(a) Original Problem (b) Homogeneous Problem

(c) Subproblem $-\alpha$ (d) Subproblem – β

Figure 5.5 Discrete system of two microslips under farfield principal stresses; decomposition of the original problem.

$$\{-\sigma_d^\beta - i[\sigma_{xy}^{\infty\beta} + \sigma_{xy}^{P\beta} - (\sigma_{yy}^{\infty\beta} + \sigma_{yy}^{P\beta} + \sigma_d^\beta)\tan\phi_c]\}dt$$
$$-\frac{1}{2\pi i\sqrt{z_\beta^2 - c_\beta^2}}\int_{-c_\beta}^{c_\beta}\frac{\sqrt{t^2 - c_\beta^2}}{t - z_\beta}\cdot$$
$$\{-i2a(\sigma_{yy}^{\infty\beta} + \sigma_{yy}^{P\beta} + \sigma_d^\beta)(\tan\phi_c - \tan\phi_0)\delta(t)\}dt, \quad \cdots\cdots (5.21)$$

$$\Psi'_\beta(z_\beta) = \overline{\Phi'_\beta(\overline{z_\beta})} - \Phi'_\beta(z_\beta) - z_\beta\Phi''_\beta(z_\beta), \quad \cdots\cdots (5.22)$$

where $\delta(t)$ is Dirac's delta function, the overbars denote complex conjugate and $z_\beta = x_\beta + iy_\beta$ with $i = \sqrt{-1}$.

From the definition of the pseudotraction, the condition that the pseudotraction must satisfy (the consistency equation) is given by

$$\sigma_{yy}^{P\alpha} - i\sigma_{xy}^{P\alpha} = \Phi'_\beta(z_\beta) + \overline{\Phi'_\beta(z_\beta)} + e^{-i2\theta_{\alpha\beta}}\{z_\beta\overline{\Phi''_\beta(z_\beta)} + \overline{\Psi'_\beta(z_\beta)}\}, \quad \cdots\cdots (5.23)$$

$$\sigma_{xx}^{P\alpha} + \sigma_{yy}^{P\alpha} = 2\{\Phi'_\beta(z_\beta) + \overline{\Phi'_\beta(z_\beta)}\}, \quad \cdots\cdots (5.24)$$

where the argument z_β is assigned to $z_\beta = d_{\alpha\beta}exp(\phi_{\alpha\beta}) + x_\alpha exp(\theta_{\alpha\beta})$, $(|x_\alpha/c_\alpha| \leq 1)$ and $d_{\alpha\beta}, \phi_{\alpha\beta}$ and $\theta_{\alpha\beta}$ are defined in Fig. 5.4.

It can be assumed that the distance between the microslips is large enough compared with half the length of the microslip, $|c_\beta/z_\beta| \ll 1$. Thus after expansion of the integrand in equation (5.21) into power series of c_β/z_β, the stress functions are expressed by

$$\Phi'_\beta(z_\beta) = -\frac{1}{4}\left(\frac{c_\beta}{z_\beta}\right)^2\{\sigma_d^\beta + i[\sigma_{xy}^{\infty\beta} + \sigma_{xy}^{P\beta} - (\sigma_{yy}^{\infty\beta} + \sigma_{yy}^{P\beta} + \sigma_d^\beta)\tan\phi_c]\}$$
$$-i\frac{ac_\beta}{\pi z_\beta^2}(\sigma_{yy}^{\infty\beta} + \sigma_{yy}^{P\beta} + \sigma_d^\beta)(\tan\phi_c - \tan\phi_0)\}, \quad \cdots\cdots (5.25)$$

$$\Psi'_\beta(z_\beta) = -\frac{1}{2}\left(\frac{c_\beta}{z_\beta}\right)^2\sigma_d^\beta, \quad \cdots\cdots (5.26)$$

where the higher order terms of (c_β/z_β) have been neglected.

Substituting equations (5.25) and (5.26) into equations (5.23) and (5.24), the consistency equation is expressed as follows:

$$\boldsymbol{\sigma}^{P\alpha} = \boldsymbol{\gamma}^{\alpha\beta}\boldsymbol{\sigma}^{\infty\beta} + \boldsymbol{\omega}^{\alpha\beta}\sigma_d^\beta, \quad (\beta \text{ not summed}), \cdots\cdots (5.27)$$

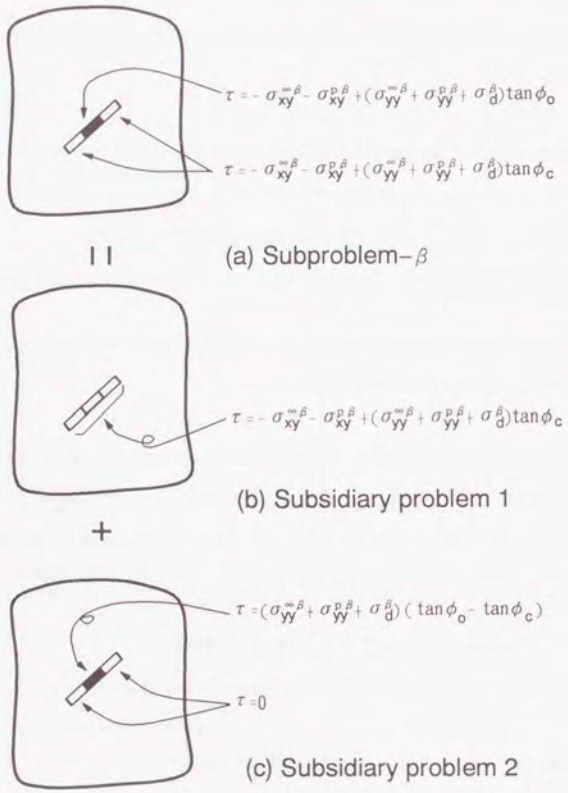

Figure 5.6 Decomposition of subproblem β.

where $\boldsymbol{\sigma}^{\infty\alpha} = \{\sigma_{xx}^{\infty\alpha}, \sigma_{yy}^{\infty\alpha}, \sigma_{xy}^{\infty\alpha}\}^T, \boldsymbol{\sigma}^{P\alpha} = \{\sigma_{xx}^{P\alpha}, \sigma_{yy}^{P\alpha}, \sigma_{xy}^{P\alpha}\}^T$,

$$[\gamma_{ij}^{\alpha\beta}] = \frac{1}{2}\left(\frac{c_\beta}{d_{\beta\alpha}}\right)^2 \begin{bmatrix} 0 & ba_1 & -a_1 \\ 0 & -ba_2 & a_2 \\ 0 & -ba_3 & a_3 \end{bmatrix} \qquad \cdots\cdots (5.28)$$

and

$$\{\omega_i^{\alpha\beta}\} = \frac{1}{2}\left(\frac{c_\beta}{d_{\beta\alpha}}\right)^2 \begin{Bmatrix} e_1 + ba_1 \\ e_2 - ba_2 \\ e_3 - ba_3 \end{Bmatrix} \qquad \cdots\cdots (5.29)$$

with

$$\begin{aligned}
a_1 &= \sin(4\phi_{\beta\alpha} - 2\theta_{\beta\alpha}) + \sin 2\phi_{\beta\alpha}, \\
a_2 &= \sin(4\phi_{\beta\alpha} - 2\theta_{\beta\alpha}) - \sin 2\phi_{\beta\alpha}, \\
a_3 &= \cos(4\phi_{\beta\alpha} - 2\theta_{\beta\alpha}), \\
e_1 &= -\cos(4\phi_{\beta\alpha} - 2\theta_{\beta\alpha}) + \cos(2\phi_{\beta\alpha} - 2\theta_{\beta\alpha}) - \cos 2\phi_{\beta\alpha}, \\
e_2 &= \cos(4\phi_{\beta\alpha} - 2\theta_{\beta\alpha}) - \cos(2\phi_{\beta\alpha} - 2\theta_{\beta\alpha}) - \sin 2\phi_{\beta\alpha}, \\
e_3 &= -\sin(4\phi_{\beta\alpha} - 2\theta_{\beta\alpha}) + \sin(2\phi_{\beta\alpha} - 2\theta_{\beta\alpha}), \\
b &= \tan\phi_c - \frac{4a}{\pi c_\beta}(\tan\phi_c - \tan\phi_0).
\end{aligned}$$

For the discrete system of two microslips, equation (5.27) gives the consistency equation which ensures the boundary condition of the original problem. For the case where several microslips exist in an elastic medium, the right hand side of equation (5.27) is changed into the summation over β (the all microslips within the elastic medium except for the microslip under consideration). Furthermore, if the microslips are continuously distributed with a certain density ρ, the effects of other microslips may be evaluated in terms of a spatial integration over the elastic medium instead of the summation over the individual microslips. In addition, the stress at infinity $\hat{\boldsymbol{\sigma}}^\infty$ in equation (5.27) is exchanged for the macroscopic stress $\hat{\boldsymbol{\sigma}}$ in the equivalent continuum. The consistency equation for the continuously distributed microslip is, as a result, given by

$$\sigma^{P\lambda}(\boldsymbol{x}) = \int_V \rho\{\gamma^{\lambda\mu}(\boldsymbol{x} \mid \boldsymbol{\xi})\dot{\sigma}^{\mu}(\boldsymbol{\xi}) + \omega^{\lambda\mu}(\boldsymbol{x} \mid \boldsymbol{\xi})\sigma_d^{\mu}(\boldsymbol{\xi})\}d\boldsymbol{\xi}, \quad (\lambda, \mu = \text{ I, II}) \cdot \quad (5.30)$$

where $\gamma^{\lambda\mu}(\boldsymbol{x} \mid \boldsymbol{\xi})$ and $\omega^{\lambda\mu}(\boldsymbol{x} \mid \boldsymbol{\xi})$ are the same definition of $\gamma^{\alpha\beta}$ and $\omega^{\alpha\beta}$ in equation (5.27), respectively, except for replacing the variables as follows:

$$\begin{aligned}
d_{\beta\alpha} &\rightarrow d = \|\boldsymbol{x} - \boldsymbol{\xi}\|, \\
\phi_{\beta\alpha} &\rightarrow \phi = \tan^{-1}\frac{x_2 - \xi_2}{x_2 - \xi_2} - \theta_{\mu}, \\
c_{\beta} &\rightarrow c_{\mu}(\boldsymbol{\xi}) \ : \text{ the microslip length in system } \mu \text{ at } \boldsymbol{\xi}, \\
\theta_{\beta\alpha} &\rightarrow \theta_{\lambda} - \theta_{\mu}.
\end{aligned}$$

where $\|\boldsymbol{u}\|$ denotes the norm of vector $\boldsymbol{u}$ and $\lambda,\ \mu = I,\ II$.

In the above formulation of the consistency equation, the microslips are assumed to be embedded in the elastic body. In actual granular materials, however, the inelastic deformation occurs all over the materials. Thus, the pseudotraction evaluated by equation (5.30) seem to be overestimated. To reduce the pseudotraction, a new constant α_r, $(0 \leq \alpha_r \leq 1.0)$ named reduced coefficient, is introduced and the consistency equation is expressed by

$$\sigma^{P\lambda}(\boldsymbol{x}) = \alpha_r \int_V \rho\{\gamma^{\lambda\mu}(\boldsymbol{x} \mid \boldsymbol{\xi})\dot{\sigma}^{\mu}(\boldsymbol{\xi}) + \omega^{\lambda\mu}(\boldsymbol{x} \mid \boldsymbol{\xi})\sigma_d^{\mu}(\boldsymbol{\xi})\}d\boldsymbol{\xi}. \quad (\lambda, \mu = \text{ I, II}) \quad (5.31)$$

Note that the case $\alpha_r = 0$ corresponds to ignoring the effects of the interaction among the microslips.

The above homogenization from the discrete system to the continuum changes the pseudotraction defined on the surface of the discrete microslips into the continuous field variable $\sigma^{P\lambda}$, $(\lambda = I, II)$, called the interaction field. In the next subsection, a evolution law for the present problem is formulated. To estimate the interaction effects of the microslips in the determination of the microslip length, the evolution law

is expressed in terms of the interaction field as well as the stress at the point where the evolution of microslip is considered.

5.3.3 Evolution law

As is the case with the evolution law for the behavior due to crack growth under compression, the damage evolution is assumed to take place as the extension of the microslip length while keeping the density of the microslip constant. The macroscopic rigidity defined in the stress–strain relation [equation (5.17)] decrease with the increase in the microslip length. Thus, the microslip length is interpreted as the damage parameter.

As a matter of fact, the microslip extension induces anisotropy in the stress–strain relation, and accordingly the direction of the principal stress varies from the direction at the initial loading stage. Nevertheless, in the following formulation, the effect of the rotation of the principal axis on the directions of the microslips is neglected for simplicity, and thereby the directions of the microslips are fixed to the same directions at the initial loading stage.

Although the microslips are considered to be distributed continuously over the homogenized equivalent continuum, we consider the single microslip at that point in the continuum in order to formulate the evolution law at a certain point in the continuum. Similarly for the treatment of the discrete system of the microslips, the problem is decomposed into a subproblem with the single microslip under consideration and the other subproblems. In the subproblem, the tractions expressed in terms of the macroscopic stress $\dot{\sigma}$ and the interaction field $\sigma^{P\lambda}$, $(\lambda = I, II)$ are applied on the surfaces of the microslip to satisfy the boundary condition. The interaction effects caused by the other microslips are estimated through the interaction field defined by equation (5.30). Then, the mode II stress intensity factor of the tips of the microslip is given by

[for system I]

$$K_{II} = \sqrt{\pi c_I}\{\hat{\sigma}^I_{xy} + \sigma^{PI}_{xy} - (\hat{\sigma}^I_{yy} + \sigma^{PI}_{yy} + \sigma^I_d)\tan\phi_c\} + \frac{2a}{\sqrt{\pi c_I}}(\hat{\sigma}^I_{yy} + \sigma^{PI}_{yy} + \sigma^I_d)(\tan\phi_c - \tan\phi_0), \quad \cdots (5.32)$$

[for system II]

$$K_{II} = \sqrt{\pi c_{II}}\{\hat{\sigma}^{II}_{xy} + \sigma^{PII}_{xy} + (\hat{\sigma}^{II}_{yy} + \sigma^{PII}_{yy} + \sigma^{II}_d)\tan\phi_c\} - \frac{2a}{\sqrt{\pi c_{II}}}(\hat{\sigma}^{II}_{yy} + \sigma^{PII}_{yy} + \sigma^{II}_d)(\tan\phi_c - \tan\phi_0), \quad \cdots (5.33)$$

where the effect of the traction applied on the initial defect has been evaluated as the concentrated force as explained in the previous subsection.

Since the stress is relaxed by the deformation of the slip zone, the stress singularity at the tips of the slip zone does not exist. This leads to the condition that the mode II stress intensity factor must be equal to zero. Consequently, the evolution law, which is the condition of the microslip extension, becomes

[for system I]

$$c_I\{\hat{\sigma}^I_{xy} + \sigma^{PI}_{xy} - (\hat{\sigma}^I_{yy} + \sigma^{PI}_{yy} + \sigma^I_d)\tan\phi_c\} + \frac{2}{\pi}(\hat{\sigma}^I_{yy} + \sigma^{PI}_{yy} + \sigma^I_d)(\tan\phi_c - \tan\phi_0) = 0, \quad \cdots (5.34)$$

[for system II]

$$c_{II}\{\hat{\sigma}^{II}_{xy} + \sigma^{PII}_{xy} + (\hat{\sigma}^{II}_{yy} + \sigma^{PII}_{yy} + \sigma^{II}_d)\tan\phi_c\} - \frac{2}{\pi}(\hat{\sigma}^{II}_{yy} + \sigma^{PII}_{yy} + \sigma^{II}_d)(\tan\phi_c - \tan\phi_0) = 0. \quad \cdots (5.35)$$

As is the case with the interaction field, the lengths of the discrete microslips are homogenized into the continuous field variable, and accordingly the above evolution law is satisfied at all points in the body.

In Table 5.1, the governing equations and unknowns of IFT are summarized. The deformation of granular materials and the evolution of the microslip are obtained by

Table 5.1 Summary of governing equations and unknowns for granular materials

equilibrium	Equation (3.22)
ε–u relation	Equation (3.23)
σ–ε relation	Equation (5.17)
evolution law	Equations (5.33) and (5.34)
consistency eq.	Equation (5.31)
unknowns	$\hat{\boldsymbol{u}}, \hat{\boldsymbol{\epsilon}}, \hat{\boldsymbol{\sigma}}, c_I, c_{II}, \boldsymbol{\sigma}^P$

solving the governing equations shown in Table 5.1 for the unknowns—the stress and strain tensors, the displacement vector, the length of the microslip and the pseudotraction. In the next section, the numerical results are shown.

5.4 Numerical Results and Discussion

The numerical procedure of IFT for the granular materials is almost the same as the procedure given in chapter 3. For the present case, however, the pseudotraction in the consistency equation (5.30) is expressed explicitly by the stress and the length of the microslip. [For the case shown in chapter 3, the consistency equation is expressed by an integral equation for the pseudotraction, and hence the explicit expression of the pseudotraction is not available; see equation (3.37).] Thus, after the pseudotraction in the evolution equations (5.34),(5.35) is eliminated by using the consistency equation, finite element method is employed for spatial discretization. The conventional triangular element with linear displacement fields is used to discretize the displacement vector and the stress and strain tensors. The damage parameters (the lengths of the microslip) are

approximate to be constant in an element and the integral in the evolution equation in which the pseudotraciton have been eliminated is evaluated numerically by Gaussian quadrature method for triangular regions.

Since there are two damage parameters (the lengths of the microslip) in a element, the discretized algebraic equations consist of $2N$ equilibrium equations and $2M$ evolution equations, where N and M are the number of the nodal points and elements, respectively. On the other hand, the unknowns for the discretized problem are $2N$–nodal displacement and $2M$–element damage parameter. Thus, we have a system of $(2N+2M)$ nonlinear equations for $(2N+2M)$ unknowns. This system of the nonlinear algebraic equations is solved by Newton–Raphson method at each stage of the loading. After the converged solution is obtained at each incremental step, eigenvalue analysis is carried out to detect the possibility of bifurcation.

As the first matter, the effects of the interaction among the microslips on the evolution of the microslip are discussed. To do this, numerical calculation is carried out for both CDM and IFT. In CDM, the interaction effects are not taken into account in determination of the microslip length and the reduced coefficient in the consistency equation (3.16) is assigned to $\alpha_r = 0$. On the other hand, the reduced coefficient of IFT is fixed to $\alpha_r = 1.0$.

The mesh configuration employed in the present calculations is displayed in Fig. 5.7, where the figures in each element denote the element number and "a" is half the length of the initial defect. The biaxial test sample consisting of 8 elements is loaded with a rigid, frictionless platen. The confining pressure on the side boundaries is loaded by the horizontal nodal forces, while the vertical load is implemented by prescribing the increment of the vertical displacement at the top boundary. The load incrementation is started from a hydrostatic stress state. After the confining pressure attained a specific value, the increment of the only displacement at the top boundary is applied. The

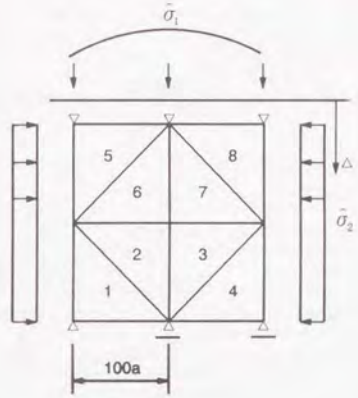

Figure 5.7 Finite element mesh for biaxial sample

model parameters used in the following numerical calculations are listed in Table 5.2.

Figure 5.8 (a) shows the relations between stress ratio $\hat{\sigma}_1/\hat{\sigma}_2$ and the normalized length of the microslip c_I/a of system I in element 1. The axial compression stress $\hat{\sigma}_1$ is calculated from the reaction of the top boundary, and thereby the stress ratio used here means the macroscopic one. For the cases of both CDM and IFT, the evolution of the microslips starts at about $\hat{\sigma}_1/\hat{\sigma}_2 = 2.7$. At initial loading stages, both the microslip lengths increase with increasing stress ratio. In CDM, the microslip length keeps increasing with further increase of the stress ratio. On the other hand, the stress ratio attains its maximum value for IFT; after that, the stress ratio decreases with increase in the microslip length.

Figure 5.8 (b) and (c) show the distribution of the microslip length at the corresponding points in Fig. 5.8 (a). In Fig. 5.8 (b) and (c), the lengths of the solid lines denote the magnitude of the microslip lengths in the elements. In CDM, all the microslip lengths are identical and distribution of microslip lengths is homogeneous throughout all loading stages; see Fig. 5.8(c). On the other hand, in IFT, at the initial

Table 5.2 Model parameters used in numerical calculation

Parameter	Value
Normalized Young's modulus	$E/\hat{\sigma}_2 = 500$
Poisson's ratio	$\nu = 0.2$
Normalized density	$\rho a^2 = 0.01$
Frictional angle of initial defect	$\phi_0 = 10$ deg
Frictional angle of slip zone	$\phi_c = 45$ deg
Dilatancy coefficient	$\alpha_d = 0.01$
	$m = 0.5$

loading stages (point A) the distribution of the microslip length is almost uniform. However, at the maximum stress ratio (point B), the microslip lengths of the elements in the diagonal direction become slightly larger than the others. Furthermore, at the descending part of the stress-damage diagram (point C), the evolution of the microslip is localized into the elements in the diagonal direction.

Figure 5.9 shows the evolution of the microslip lengths in all elements by IFT. The uniformity in the evolution of the microslips is lost even at the early stages of loading before the maximum stress ratio. From the loading stage just before the maximum stress ratio, the microslip lengths decrease in several elements.

The numerical results presented here confirm that IFT for granular materials can reproduce localization phenomena as well as softening behavior, while in CDM localization of damage does not occur and there is no critical stress ratio. In IFT, it is also shown that nonhomogeneous evolution of damage starts at an early loading stage before the critical stress ratio. This feature agrees with the localization process of the

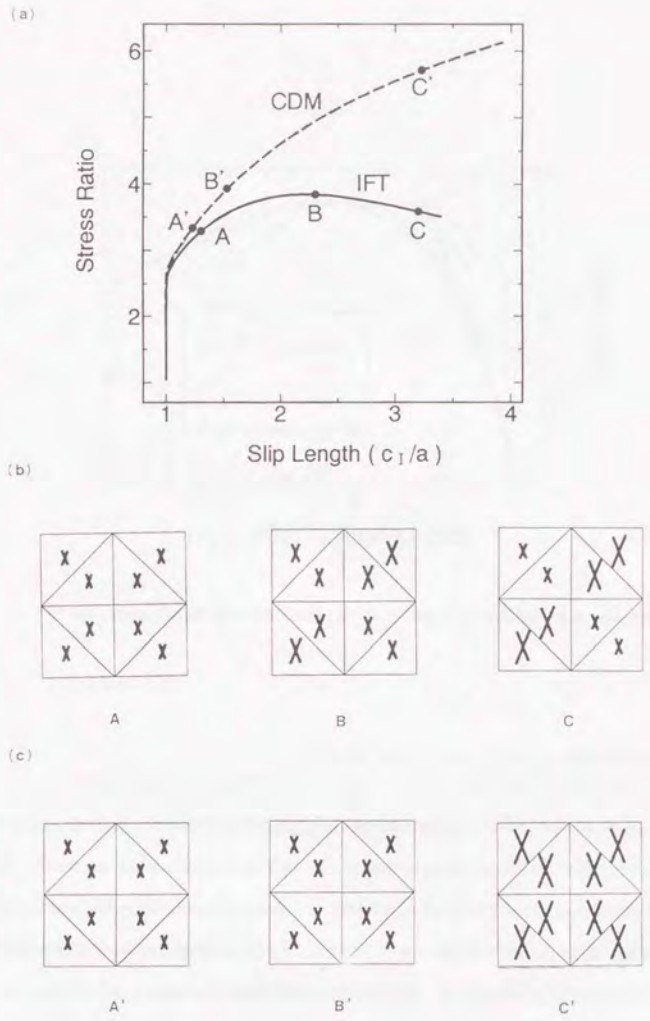

Figure 5.8 Effects of interaction on evolution of microslip: (a) Stress ratio vs normalized microslip length of element 1; Distribution of microslip length for (b)IFT; (c)CDM.

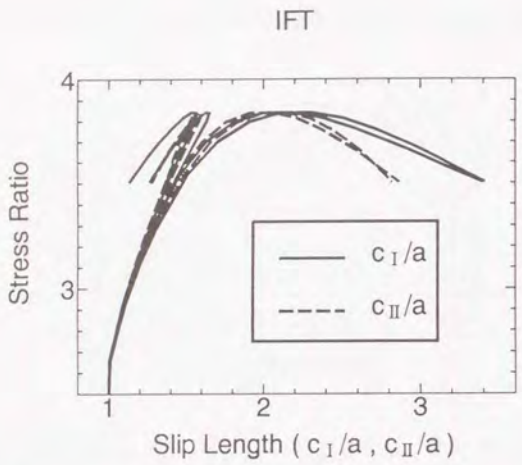

Figure 5.9 Evolution of microslip lengths (damage parameters) for IFT.

shear band formation observed in sand samples.

Figure 5.10 shows stress–strain relation evaluated by IFT, in which the axial strain is calculated from the axial displacement of the top boundary of the finite element mesh. The inelastic strain calculated by IFT is considerably smaller than experimental results observed in actual samples of sand. This underestimation is probably due to as follows. In a actual sand sample, the inelastic deformation occurs all over the sample owing to a change of void with rearrangement of the grains. while in the theoretical model considered here the inelastic strain is calculated from the summation of the displacement gaps of the microslips embedded in the elastic medium. The inelastic strain of actual sand is considered to be generated by plastic-like process rather than by effect of a specific microstructure.

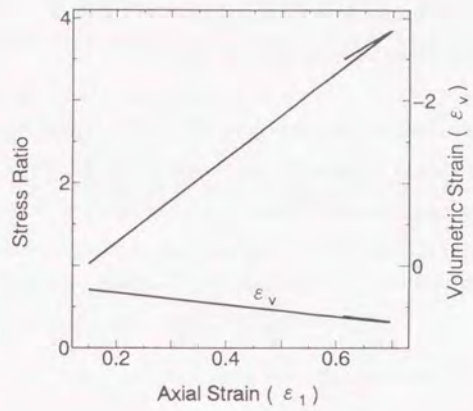

Figure 5.10 Stress–strain relation for IFT

5.5 Summary

In this chapter, an application of IFT to granular materials under compressive stress state is presented. To formulate the governing equations of IFT, the microslip model is adopted, in which inelastic deformation of granular materials from a microscopic point of view is reflected. The procedure of the formulation presented in this chapter is the almost same as that in chapter 3. The elastic medium containing many microslips is homogenized into an equivalent continuum. In this homogenization process, special attention is placed on the consideration of the interaction effects among the microslips on the determination of the microslip length (damage parameter). The numerical examples are shown for both IFT and CDM to examine the effects of interaction on the evolution of the microslips. (In this paper, a version of IFT in which the interaction effects are not taken into account is referred to as CDM.)

Although CDM cannot reproduce localization phenomena, the numerical results confirm that IFT can simulate localization phenomena and damage-softening behavior. This result suggests that one of the main mechanism of strain localization is the effects of interaction among microdefects existing in materials.

The inelastic deformation calculated from IFT is considerably smaller than the experimental results observed in actual sand samples. Although the mechanism of localization phenomena is explained by the micromechanics-based method, the micromechanics-based formulation of the stress–strain relation is not suitable for granular materials.

References

J. P. Bardet and J. Proubet [1991], A numerical investigation of the structure of persistent shear bands in granular media. *Géotechnique*, 41(4):599–613.

R. Butterfield, R. M. Harkness, and K. Andrawes [1970], A stereo-photogrammetric method for measuring displacement fields. *Géotechnique*, 20(3):308–314.

P. A. Cundall [1989], Numerical experiments on localization in frictional materials. *Ingenieur-Archiv* , 59:148–159.

A. Drescher, I. Vardoulakis and C. Han [1990], A biaxial apparatus for testing soils. *Geotechnical testing journal ASTM* , 13(3):226–234.

W.-K. Lam and F. Tatsuoka [1988], Effects of initial anisotropic fabric and σ_2 on strength and deformation characteristics of sand. *Soils and Foundations*, 28(1):89–106.

G. Mandel, L. N. J. de Jong and A. Maltha [1977], Shear zones in granular material. *Rock Mech.*, 9:95–144.

D. Negussey and Y. P. Vaid [1990], Stress dilatancy of sand at small stress ratio states. *Soil and Foundations*, 30(1):155–166.

L. Rothenburg and R. J. Bathurst [1989], Analytical study of induced anisotropy in idealized granular materials. *Géotechnique*, 39(4):601–614.

Z.-H. Shi and H. Horii [1989], Microslip model of strain localization in sand deformation. *Mech. Mater.*, 8:89–102.

F. Tatsuoka, M. Sakamoto, T. Kawamura and S. Fukushima [1986], Strength and deformation characteristics of sand in plane strain compression at extremely low pressures. *Soils and Foundations*, 26(1):65–84.

F. Tatsuoka, S. Nakamura, C. -C. Huang, and K. Tani [1990], Strength anisotropy and shear band direction in plane strain test of sand. *Soils and Foundations*, 30(1):35–54.

I. Vardoulakis and B. Graf [1985], Calibration of model for granular materials using data from biaxial experiments. *Géotechnique*, 35(3):299–317.

W. Wu and D. Kolymbas [1991], On some issues in triaxial extension tests. *Geotechnical Testing Journal ASTM* ,14(3):276–287.

T. Yoshida [1992], *Observations on shear bands in sands during plane strain compression test.* Master's thesis, Institute of Industrial Science University of Tokyo. in Japanese.

Chapter 6

Summary and Conclusions

6.1 Summary

A micromechanics-based continuum theory, named Interaction Field Theory (IFT), was proposed. The present theory is intended to reproduce localization phenomena, which are difficult to model by conventional Continuum Damage Mechanics (CDM). The main feature that distinguishes IFT from CDM is the direct evaluation of the effects of interaction among microdefects in materials. To take account of the interaction effects in the determination of evolution of damage, an additional field variable named interaction field was introduced and the governing integral equation was formulated.

The summary of the chapters in this paper is as follows.

[Chapter 1]

The localization phenomena discussed in this paper were introduced. A survey was done on the theoretical work for mechanics of localization.

[Chapter 2]

The basic concept of IFT was illustrated through comparison with conventional CDM based on micromechanics.

[Chapter 3]

The formulation of IFT was carried out for rate-independent behaviors of brittle materials with microdefects under compression. In addition, to compare with conventional CDM, a CDM based on micromechanics was also formulated for the same problem. The numerical results were presented for both IFT and CDM. The efforts were made to predict the strengths of actual rocks under compressive stress state.

[Chapter 4]

IFT was applied for time-dependent behavior of brittle materials. The numerical results were given, which were intended to reproduce creep tests of Barre granite under constant stress states.

[Chapter 5]

IFT was formulated for granular materials under compressive stress states. The microslip model was employed as the micromechanical model which represent the behaviour of the granular materials. The numerical calculation was carried out to clarify effects of the interaction among microslips as well as the model parameters on the numerical results. The applicability of IFT for granular materials was discussed.

6.2 Conclusions

[Chapter 1]

From a literature survey on the theoretical work done, the reason why conventional

CDM cannot reproduce localization phenomena was investigated. In addition, even if continuum theories are employed to be able to reproduce localization phenomena, complication resulting from using such theories in numerical simulation for localization phenomena (mesh dependency of numerical results) was shown and the proposed conventional countermeasures were classified.

[Chapter 2]

It was shown that, by considering the effects of interaction among microdefects, the constitutive relation depends on the stress and the damage parameter at all points within the material. This nonlocality is introduced inevitably into the continuum theory for materials containing microstructure and it has also been clarified that a mechanical meaning of nonlocality is the interaction effects.

[Chapter 3]

In the conventional nonlocal theory, justification of the attenuation functions and associated internal characteristic length were mainly checked by phenomenological consideration based on numerical simulations. Thus, it seems that the conventional attenuation functions were introduced as only a technique of numerical calculations and the justification is not clarified. However, in the present formulation, the attenuation function for the considered model of the microdefect is derived rigorously with the method of micromechanics.

The numerical results confirm that IFT is able to simulate localization phenomena as well as softening behaviors. Furthermore, it was shown that IFT can reproduce the transition from an axial splitting failure into a shear failure, which is observed in triaxial test of actual brittle rocks as the confining pressure is increased.

The failure envelopes of actual rocks under compression were predicted by IFT. For Westerly granite, the predicted result is plausible for confining pressure ranging from 20

to 600 MPa, in which the shear failure mode occurs as the macroscopic failure. When the confining pressure is greater than 600 MPa, the predicted failure envelope deviated from experimental data. This results suggests that, for this range of the confining pressure, plastic deformation governs the macroscopic failure instead of microcracking.

The strengths of other kinds of rocks under compression were also estimated. Since all model parameters necessary for calculations were not available, the parameters such as the density of microdefects and the frictional coefficients were determined so as to fit the numerical results to the experimental data. Although the comparison should not necessarily be regarded as a direct support of the ability of the present theory owing to some arbitrary parameters, it seems that the values of the determined parameters are within the reasonable range for the intended applications.

[Chapter 4]

It was shown that IFT reproduces typical behavior of creep deformation observed in laboratory tests; namely, the primary, secondary and tertiary stages of creep deformation. This suggests that the mechanisms of these three stages of the creep deformation are reasonably explained by the present theory. In the primary creep, the crack lengths increase rapidly, because the stress intensity factor is nearly equal to the fracture toughness. The transition from the primary stage into the secondary one results from the fact that, for the considered micromechanical model, the stress intensity factor decreases with increasing the crack length under constant stress states. As the cracks grow further, the effects of interaction among microdefects on the crack growth become dominant and thereby the crack growth in certain zones is accelerated, which is the main mechanism of steep increase in strain during the tertiary creep.

In the numerical calculation, the eventual macroscopic failure following the tertiary creep is reproduced by unstable increase in crack lengths (damage parameters). The time to failure decreases with increasing the normalized stress difference, which

tendency agrees with experimental results.

[Chapter 5]

IFT for granular materials reproduces localization phenomena, such as shear band formation observed in actual sand samples under compressive stress states. In addition, the damage softening behavior is simulated. However the inelastic deformation calculated by IFT is considerably smaller than experimental results observed in plane compression test of actual sands.

6.3 Future Directions

The major work done in this research is to develop a continuum theory for localization phenomena in the framework of a micromechanics-based approach. In addition, the mathematical structure of the continuum theory ruled out phenomenological features as much as possible was discussed. Since there is a lot of future improvements in the proposed theory from the practical point of view, the proposed theory may be regarded as a trial theory rather than a practically usable one. However, even in formulation of practical theories, it is important to consider the mathematical structure resulted from micromechanics-based formulation, because the merely phenomenological approach often brings about no essential structure.

In the following, the improvements in the present theory from practical point of view are given, in which the formulation based on more or less phenomenological consideration is needed.

(a) Effect of plasticity and finite deformation

As mentioned in section 3.6 and 5.4, it is necessary that the effect of the plastic defor-

mation of matrix is taken into account in order to consider the behaviors of sand and even rocks under high confining pressure. Moreover, to describe the coupling behavior of plasticity and damage due to microdefects, the problem should be formulated with deformation theory considering geometrical nonlinearity. In fact, the continuum theory in which both microcracking and plasticity are considered as sources of the inelastic deformation has been proposed by Dragon and Mróz [1979]. In the present theory, the estimation of the effects of interaction among microdefects is based on the principle of superposition, in which the matrix of materials is assumed to be linear elastic. Thus, it is difficult to include the effects of plasticity and geometrical nonlinearity in the straightforward way. However, if the principle of the superposition is assumed to hold within incremental or rate quantities such as the Jaumann rates, the consistency equation can be rewritten for the rates, and thereby these effects can be taken into account.

(b) Effect of rotation of the principal axis

To simulate behavior of materials under complex loading paths including the rotation of the axis of principal stresses, the effect of the rotation on the orientation of microdefects must be considered. Even if the rotation of the principal axis due to external loading does not induced, once the localization of deformation occurs, the distribution of stress varies. Accordingly the direction of the principal stress is changed from that at the initial loading stage. In the present theory, the effect of the rotation of principal axis on the orientation of microdefects is neglected for simplicity. The orientation of microdefects is fixed to the same orientation as that at initial loading stage. On of the methods of considering this effect is to express the damage parameter as a tensor field instead of the scalar field considered in the present theory. Another method which have been proposed to consider this effect is to introduce the probability density function for the orientation of microdefects. The introduction of the tensorial damage parameter and the probability density function has been reported by Murakami [1983] and Wohua

and Valliappan [1990a,b], respectively.

Apart from practical poit of view, one of issues of interest is the selection of the solution paths. As with other continuum theories which can reproduce localization phenomena, the present theory reproduces localization phenomena as bifurcation of the solution path. At the bifurcating point, the uniqueness of the solution does not hold and the stability of the solution is changed. In the framework of plasticity, Hill [1958] presented the conditions for uniqueness and stability of boundary-value problem of rate-independent solids. Recently, Nguyen [1985, 1987] presented an alternative formulation of these conditions for the evolution of a class of generalized standard systems in which the irreversible process is characterized by normality and convexity in the context of thermomechanics (not in the context of plasticity). This class includes not only classical plasticity but also crack extension in brittle solids and brittle damage [see also Maugin, 1992]. It is necessary to consider this type of stability criterion based on thermomechanics in order to examine rigorously which of the solution paths are selected at bifurcation points. An extension of the present study to include the stability criterion will be of further interest.

References

A. Dragon and Z. Mróz [1979], A continuum model for plastic-brittle behaviour of rock and concrete, *Int. J. Engng. Sci.*, 17:121–137.

R. Hill [1959], A general theory of uniqueness and stability in elastic–plastic solids. *J. Mech. Phys. Solids*, 6:236–249.

Q. S. Nguyen [1985], Uniqueness, stability and bifurcation of standard systems. In A. Sawczuk and G. Bianchi editors, *Plasticity Today*, pages 399–412, Elsevier, London and New York.

Q. S. Nguyen [1987], Bifurcation and post-bifurcation analysis in plasticity and brittle fracture. *J. Mech. Phys. Solids*, 3:303–324.

G. A. Maugin [1992], *The Thermomechanics of Plasticity and Fracture*, Cambridge Univ. Press, Cambridge.

S. Murakami [1983], Notion of continuum damage mechanics and its application to anisotropic creep damage theory, *J. Engng. Mater. and Tech.* 105:99–105.

Z. Wohua and S. Valliapan [1990a], Analysis of random anisotropic damage mechanics problem of rock mass: Part I – Probabilistic simulation, *Rock Mech. and Rock Engng.*, 23:91–112.

Z. Wohua and S. Valliapan [1990b], Analysis of random anisotropic damage mechanics problem of rock mass: Part II – Statistical estimation, *Rock Mech. and Rock Engng*, 23:241–259.